



Science Arts & Métiers (SAM)

is an open access repository that collects the work of Arts et Métiers Institute of Technology researchers and makes it freely available over the web where possible.

This is an author-deposited version published in: <https://sam.ensam.eu>
Handle ID: <http://hdl.handle.net/10985/21521>

To cite this version :

T. LAVIGNE, Giuseppe SCIUMÈ, Sébastien LAPORTE, Helene PILLET, Stéphane URCUN, B. WHEATLEY, Pierre-Yves ROHAN - Numerical investigation of the time-dependent stress-strain mechanical behaviour of skeletal muscle tissue in the context of pressure ulcer prevention - Clinical Biomechanics p.105592 - 2022

Any correspondence concerning this service should be sent to the repository

Administrator : scienceouverte@ensam.eu



Numerical investigation of the time-dependent
stress-strain mechanical behaviour of skeletal muscle
tissue in the context of Pressure Ulcer prevention

T. Lavigne^{a,b,*}, G. Sciumè^b, S. Laporte^a, H. Pillet^a, S. Urcun^{a,b,c}, B.
Wheatley^d, P-Y. Rohan^a

^a*Arts et Metiers Institute of Technology, IBHGC, 151 bd de
l'hôpital, Paris, 75013, France*

^b*Arts et Metiers Institute of Technology, Univ. of Bordeaux, CNRS, Bordeaux INP,
INRAE, I2M Bordeaux, Avenue d'Aquitaine, Pessac, 33607, France*

^c*Institute for Computational Engineering Sciences, Department of Engineering Sciences,
Faculte des Sciences, de la Technologie et de Medecine, Universite du
Luxembourg, Campus Kirchberg, 6, rue*

Coudenhove-Kalergi, Luxembourg, L-1359, Luxembourg

^d*Department of Mechanical Engineering, Bucknell University, 1 Dent
Drive, Lewisburg, 17837, Pennsylvania, USA*

Abstract

Background: Pressure-induced tissue strain is one major pathway for Pressure Ulcer development and, especially, Deep Tissue Injury. Biomechanical investigation of the time-dependent stress-strain mechanical behaviour of skeletal muscle tissue is therefore essential to understand and prevent the onset of Deep Tissue Injury. In the literature, a viscoelastic formulation is generally assumed for the experimental characterization of skeletal muscles, with the limitation that the underlying physical mechanisms that give rise to the time dependent stress-strain behaviour are not known. The objective of this study is to explore the capability of poroelasticity to reproduce the apparent viscoelastic behaviour of passive muscle tissue under confined compression.

Methods: Experimental stress-relaxation response of 31 cylindrical porcine samples tested under fast and slow confined compression by Vaidya and collaborators were used. An axisymmetric Finite Element model was developed in ABAQUS and, for each sample a one-to-one inverse analysis was performed to calibrate the specimen-specific constitutive parameters, namely, the drained Young's modulus, the void ratio, hydraulic permeability, the

37 Poisson's ratio, the solid grain's and fluid's bulk moduli.
38 *Findings:* The peak stress and consolidation were recovered for most of the
39 samples (N=25) by the poroelastic model (normalised root-mean-square er-
40 ror ≤ 0.03 for fast and slow confined compression conditions).
41 *Interpretation:* The strength of the proposed model is its fewer number of
42 variables (N=6 for the proposed poroelastic model versus N=18 for the vis-
43 cohypereelastic model proposed by Vaidya and collaborators). The incorpo-
44 ration of poroelasticity to clinical models of Pressure Ulcer formation could
45 lead to more precise and mechanistic explorations of soft tissue injury risk
46 factors.
47 *Keywords:* pressure ulcer, load-tolerant soft tissues, muscle passive
48 behaviour, viscoelasticity, poroelasticity

49 **Count of words. Abstract: 260; Manuscript: 3611.**

50 1. Introduction

51 Pressure Ulcers (PUs) have been defined in the 2019 Clinical Practice
52 Guideline (CPG) published jointly by the European Pressure Ulcer Advisory
53 Panel (EPUAP), the National Pressure Injury Advisory Panel (NPIAP), and
54 the Pan Pacific Pressure Injury Alliance (PPPIA) as "*localized injuries to the*
55 *skin and underlying soft tissue that form during prolonged exposure to me-*
56 *chanical loads*" (Gefen et al. [1]). These usually occur over a bony prominence
57 but may also be related to the interaction between the skin and an external
58 medical device such as, for example, when patients interact with medical
59 devices (orthoses, prostheses, manual wheelchair, etc) or support surfaces
60 (Gefen et al. [2]). Despite long-standing risk assessment scales and man-
61 agement strategies, the relative high incidence of PUs, **and especially Deep**
62 **Tissue Injuries (DTI)**, requires extensive treatment representing a significant
63 financial burden on health services throughout the world (Bennett et al. [3]).

64 Over the past 20 years, research has sought to explain soft tissue in-
65 jury risk factors in terms of the local mechanical environment within soft
66 tissues. Of particular interest are the series of experiments performed at
67 the Eindhoven University of Technology (Ceelen et al. [4], Loerakker et al.

*Corresponding author

Email address: `thomas.lavigne@ensam.eu` (T. Lavigne)

[5], Stekelenburg et al. [6], van Nierop et al. [7], Traa et al. [8]) involving indentation of the tibialis anterior muscle of Brown-Norway rats that lead to identify a damage threshold for healthy murine skeletal muscle tissue. Using dedicated organ-scale Finite Element models, it was shown that direct deformation damage was apparent only when a given maximum Green-Lagrange shear strain threshold was exceeded (Ceelen et al. [4]), and that the damaged area was correlated to the magnitude of the elastic strain energy applied (Loerakker et al. [9]).

To interrogate individual soft tissue injury risk based on the evaluation of the local mechanical state, tissue-scale Finite Element models of load-bearing soft tissue in humans have been developed. These have consistently shown that bony prominence in the buttock (Linder-Ganz et al. [10, 11, 12], Luboz et al. [13], Moerman et al. [14], Macron et al. [15]), the foot (Bucki et al. [16], Niroomandi et al. [17], van Zwam et al. [18]) and at the stump-socket interface (Portnoy et al. [19], Dickinson et al. [20], Ramasamy et al. [21]) induce substantial stress concentrations (generally in skeletal muscles), which explains why these areas are vulnerable to ulceration.

Studies in the literature however are generally conducted with the assumption of quasi-static loading and response (Al-Dirini et al. [22]). Yet, the knowledge of the local mechanical condition alone is not sufficient to predict tissue damage initiation. The major limitation is that tissue damage is governed by a number of coupled biological and physical processes that occur at different spatial scales and often have very different temporal characteristics. Hence, the loading history is essential, because the time that a tissue is subjected to a sustained compression is a major determinant of tissue damage. It follows that the biomechanical investigation of the time-dependent stress-strain mechanical behaviour of soft tissues, and in particular, of skeletal muscle tissue, is essential to **improve the understanding of the onset of DTI and therefore would allow a better prevention.**

Attempts to characterise the time-dependence of skeletal muscle tissue generally assume a viscoelastic formulation and typically ignore the bi-phasic nature of the tissue (Van Looke et al. [23], Simms et al. [24], Wheatley et al. [25]). In the case of viscoelasticity, the underlying physical mechanisms that give rise to the time dependent stress-strain behavior are not taken into account mechanistically. Yet, it is known that skeletal muscles are composed of a porous solid matrix (muscle fibers and extracellular matrix) filled with fluid (approximately 75% bound and free fluid Sjogaard and Saltin [26]). The overall mechanical behavior of these tissues depends not only on the

106 solid matrix deformation, but also on the movement of the fluid within the
107 pores during the deformation. Since fluid plays a role in the load transfer in
108 these tissues, it follows that the stress-strain behavior of these tissues will be
109 time dependent.

110 Many research teams have proposed using poroelastic constitutive mod-
111 els as an alternative to visco-elastic models to capture the history-dependent
112 response of soft tissues under static and dynamics loading (Gimnich et al.
113 [27], Argoubi and Shirazi-Adl [28], Peyrounette et al. [29], Siddique et al.
114 [30], Hosseini-Farid et al. [31], Franceschini et al. [32], Sciumè et al. [33]).
115 A comparison between visco-elastic and poro-elastic framework given in Ap-
116 pendix C. Porous media models also represent a promising approach for
117 the integration of multiscale/multiphysics data to probe biologically rele-
118 vant phenomena at a smaller scale and embed the relevant mechanisms at
119 the larger scale (in particular, biochemistry of oxygen and of inflammatory
120 signalling pathways), allowing the interpretation of the different time char-
121 acteristics (Urcun et al. [34], Sciumè et al. [35], Sciumè [36], Gray and Miller
122 [37], Mascheroni et al. [38]).

123 In a previous study, Vaidya and Wheatley [39] have tested porcine Tibialis
124 Anterior (TA) muscle samples under fast and slow Confined/Unconfined com-
125 pression and have proposed a robust hyper-viscoelastic model to numerically
126 reproduce the mechanical behaviour in compression based on four loading
127 conditions. Building upon this experimental work, the aim of the presented
128 study is to explore the capability of poroelasticity to reproduce the apparent
129 viscoelastic behaviour of passive muscle tissue under Confined Compression
130 and to investigate the contribution of extracellular fluid flow.

131 2. Methods

132 2.1. Experimental data

133 This study was based on the experimental stress relaxation results of
134 porcine muscle samples tested under fast and slow confined compression
135 in Vaidya and Wheatley [39] (Figure 1 (a, b, c)). Briefly, thirty-one cylin-
136 drical muscle porcine samples (average height 7.03 mm and average radius
137 3.2 mm) were compressed in an impermeable steel well (diameter=6.9 mm,
138 depth=8 mm), using a uniaxial tabletop Instron 3366 tensile testing system
139 equipped with an Al₂O₃ porous plunger (diameter=6.4 mm, length=25.5
140 mm, Figure 1 (a)). Two stress relaxation testing conditions were used. Spec-
141 imens were strained to 15% at two different strain rates: a fast compression

142 at $15\% \text{ s}^{-1}$ (n=16 cylinders) and a slow compression at $1.5\% \text{ s}^{-1}$ (n=15 cylinders). They were maintained at this strain level during 400s (Figure 1 (c)).
 143
 144 All tests were completed under transverse compression to simulate the most
 145 common uniaxial physiological loading orientation.

146 A visco-hyper-elastic model was calibrated in Vaidya and Wheatley [39]
 147 using unconfined and confined fast compression data concurrently. This constitutive model was based on an uncoupled Yeoh hyperelastic formulation
 148 and a four cell Maxwell viscoelastic model (four term Prony series). The
 149 results obtained are recalled in Table 1.
 150

Law	Parameters Type	Parameter symbol	Value
Yeoh	Hyper-elastic (MPa)	C_{10}, C_{20}, C_{30}	$2.23 \cdot 10^{-5}, 1.28 \cdot 10^{-4}, 2.52 \cdot 10^{-5}$
	Hyper-elastic (MPa^{-1})	D_1, D_2, D_3	105.9, 0.839, 0.0
Prony Series	Shear Coefficients (-)	G_1, G_2, G_3, G_4	0.741, 0.086, 0.093, 0.061
	Bulk Coefficients (-)	K_1, K_2, K_3, K_4	0.563, 0.150, 0.108, 0.147
	Time Coefficients (s)	$\tau_1, \tau_2, \tau_3, \tau_4$	0.05, 1, 20, 400

Table 1: Hyper-elastic and viscoelastic parameters of the finite element model calibrated using unconfined and confined fast compression data concurrently [39]

151 The present study focuses on the Confined Compression case, but future
 152 work will extend the work to the Unconfined Compression case.

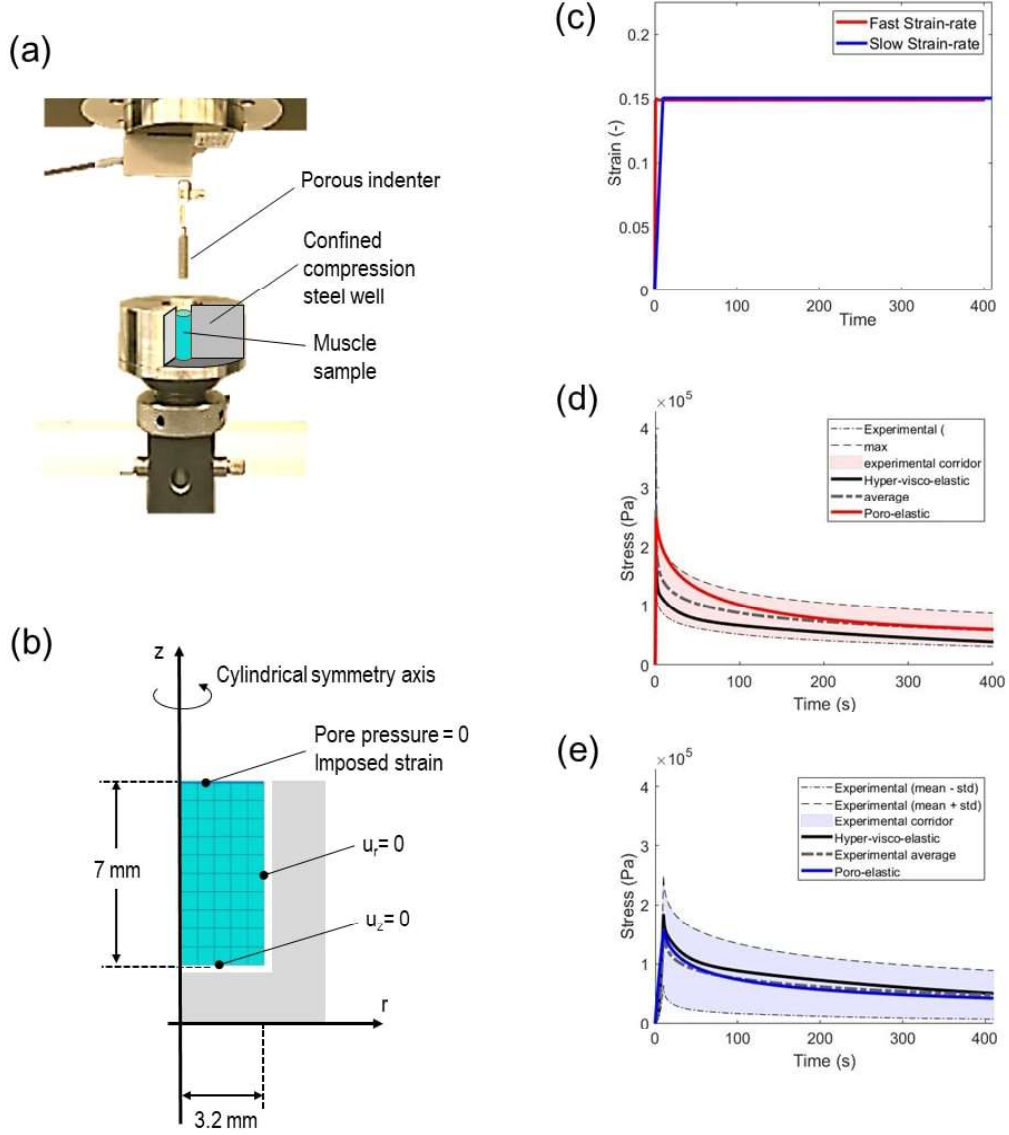


Figure 1: Experimental set up for Confined Compression (a) with its schematic representation of the finite element model (b) and imposed strain law (c) from Vaidya and Wheatley [39]. Results for the fast strain-rate (d) and for the slow strain-rate (e) average experimental relaxation curve calibration. The experimental corridor of the campaign of Vaidya and Wheatley [39] is light red for the fast strain rate and light blue for the slow one, the average experimental stress is in dashed grey. The visco-hyper-elastic model calibrated in Vaidya and Wheatley [39] is in black while poroelastic model predictions with a Poisson's ratio of 0.4879 are in red for the fast strain rate and blue for the slow strain-rate.

153 2.2. Finite Element Modeling

154 A poro-elastic mathematical model was implemented in the general pur-
 155 pose Finite Element software ABAQUS (ABAQUS, 2019) and an inverse
 156 analysis was performed to fit a quasi-incompressible, isotropic, poroelastic
 157 constitutive model (solid saturated by an incompressible viscous fluid) to re-
 158 produce the mean experimental mechanical response (stress relaxation). For
 159 more details on the theoretical basis of the model, the reader is referred to
 160 Appendix B. The modelling procedure followed complies with the consensus
 161 process that started within the Editorial Board of Clinical Biomechanics, and
 162 published by Viceconti and collaborators Viceconti et al. [40].

163 In this work, inertial and gravitational forces were neglected. It was also
 164 assumed that there is no blood flux in the samples since the experimentation
 165 was performed *ex vivo* on small samples. Muscle tissue was therefore assumed
 166 to be a mixture of two phases, an interstitial fluid and the solid scaffold. The
 167 porous medium was assumed to be fully saturated.

168 A preliminary study for small deformation case was carried out to assess
 169 the reliability of our formulation, comparing to the Terzaghi analytic solution
 170 (see Appendix D).

171 Then, a 2D axisymmetric model was proposed for the Confined Compres-
 172 sion test (n=50 CAX4PH elements: 4-node bi-linear displacement and pore
 173 pressure, hybrid with constant pressure), as illustrated in Figure 1 (b).

174 The definition of the constitutive laws was defined as follows. The solid
 175 phase behaviour was assumed linear elastic (eq. B.11). Hence, it was gov-
 176 erned by its Young's modulus, E , and Poisson's ratio, ν . The pore fluid was
 177 assumed to follow Darcy's law as presented before, and was approximated
 178 by the Forchheimer's law of Abaqus [41] (eq. 1) . Finally, the model was
 179 completed by the definition of the bulk moduli of solid grain, K^s , and of the
 180 fluid, K^l .

$$s\varepsilon^l \mathbf{v}^l = -\tilde{k} \cdot \left(\frac{\partial p}{\partial \mathbf{x}} \right) \quad (1)$$

$$\tilde{k} = \frac{k^\varepsilon}{\mu^l} \quad (2)$$

181 Where \tilde{k} denotes the hydraulic permeability depending on the void ratio, $e = \frac{\varepsilon^l}{1-\varepsilon^l}$. \mathbf{v}^l is
 182 the fluid velocity. Finally, p is the wetting liquid pore pressure, s the fluid saturation of
 183 the porous medium.

184 Boundary conditions are recalled in Figure 1 (b). As it was defined in the
 185 previous section, two types of boundary conditions were defined. Displace-
 186 ment BC were imposed on the top surface at the several strain rates. A pore
 187 pressure equal to zero was imposed on the fluid leaking surfaces. Displace-
 188 ment was vertically locked on the bottom surface and radially locked on the
 189 lateral surface.

190 Once the material was defined, three analysis steps were created. Dur-
 191 ing the first step, only the displacement boundary conditions were defined.
 192 Additionally, an initial void ratio of the porous medium was defined. Then,
 193 the displacement load was applied during a compression step, and the pore
 194 pressure boundary condition was added. Finally, the imposed displacement
 195 was sustained so as to observe the stress relaxation during 400s. For these
 196 two last steps, the soil formulation proposed by ABAQUS was used with an
 197 iterative resolution scheme due to the high strains. The duration of the steps
 198 were provided according to Vaidya and Wheatley [39] experiments and an
 199 automatic time step was considered.

200 2.3. Model Calibration

201 The mean experimental stress relaxation curve of confined compression
 202 were fitted using the `@lsqnonlin()` function of Matlab (Matlab R2019a) and
 203 its 'Trust-reflective' algorithm. Specifically, we used Matlab to call ABAQUS
 204 with an initial **estimate** for the material model parameters, performed a for-
 205 ward simulation in ABAQUS, read the simulation-based output forces in
 206 Matlab, computed a custom error metric J (eq. 6) computing the error over
 207 the peak stress (eq. 3), the area between the curves (eq. 5) and the final slope
 208 of the curve (eq. 4) (over the 50 last seconds). This process was repeated
 209 iteratively until reaching the cost function local minimum.

210 As the algorithm 'Trust-region-reflective' of the least square minimisation
 211 function is based over gradients, it is more sensitive to the initial **estimate**,
 212 and a high number of parameters increase the risks of local minimums. A
 213 preliminary calibration was therefore run over the averaged stress-time exper-
 214 imental curve considering the 6 parameters of our model (E , ν , e , \tilde{k} , K^s , K^l).
 215 In order to minimize the risk of local minimums during the calibration proce-
 216 dure, the following parameters were assigned the value obtained during this
 217 preliminary calibration : $\nu = 0.4879$ and $K^s = 0.799\text{MPa}$. $K^l = 2.2\text{GPa}$ was
 218 assumed to be equal to the water bulk modulus. The one-to-one calibration
 219 was therefore performed on the following subset of parameters : E , e , \tilde{k} .

$$J_1 = \frac{1}{3} \cdot \left(\frac{\max(\mathbf{t}_{abq}^{tot}) - \max(\mathbf{t}_{exp}^{tot})}{\max(\mathbf{t}_{exp}^{tot})} \right)^2 \quad (3)$$

$$J_2 = \frac{1}{3} \cdot \left(\frac{\frac{\partial \mathbf{t}_{abq}^{tot}}{\partial t} - \frac{\partial \mathbf{t}_{exp}^{tot}}{\partial t}}{\frac{\partial \mathbf{t}_{exp}^{tot}}{\partial t}} \right)^2 \quad (4)$$

$$J_3 = \frac{1}{3} \cdot \left(\frac{rms(\mathbf{t}_{abq}^{tot} - \mathbf{t}_{exp}^{tot})}{norm(\mathbf{t}_{exp}^{tot})} \right)^2 \quad (5)$$

$$J = J_1 + J_2 + J_3 \quad (6)$$

Where \mathbf{t}_{abq}^{tot} is the stress-time solution of ABAQUS, \mathbf{t}_{exp}^{tot} is the experimental stress-time curve, $\frac{\partial \bullet}{\partial t}$ is the derivative over the last points of the data, $rms()$ and $norm()$ are respectively the root mean square and norm functions of matlab.

The samples' size, '.inp' ABAQUS files and python routines for ABAQUS are provided to the reader in Appendix A.

3. Results

3.1. Sensitivity to mesh and initial *estimate*

A mesh analysis was conducted. Due to the simplicity of the geometry of the sample, little variation was observed depending on the seeding. Three seeding were considered: 50 dof, 105 dof and 180 dof. These different seeding of the mesh led to negligible change in the mechanical response (quantitatively, the cost function was unchanged and equal to 0.0061).

Another sensitivity study was carried out over the initial parameter *estimates*. Two initial *estimates* have been considered for the Young's modulus E , void ratio e and hydraulic permeability \tilde{k} : [$E = 17989\text{Pa}, e = 0.6996, \tilde{k} = 6.07 \cdot 10^{-14}\text{m}^2\text{Pa}^{-1}\text{s}^{-1}$] *vs.* [$E = 8995\text{Pa}, e = 0.3498, \tilde{k} = 3.035 \cdot 10^{-14}\text{m}^2\text{Pa}^{-1}\text{s}^{-1}$]. The error metrics varied between 0.0061 and 0.0084 respectively. This difference of the cost function is discussed in the section 4.

3.2. Calibration of the average experimental relaxation curve

The result of the calibration of the average relaxation stress-time curve is superimposed in Figure 1 (d, e) onto the average experimental sample stress-time curve and the experimental corridor. The calibrated visco-hyper-elastic

numerical model reported in Vaidya and Wheatley [39] is also superimposed for the ease of comparison.

The parameters identified were, respectively, for fast and slow strain-rate: Young's modulus of 22 kPa, Poisson's ratio of 0.4879, void ratio e of 0.85 (which corresponds to a porosity of 46%) and hydraulic permeability of $\tilde{k} = 4.49 \cdot 10^{-14} \text{ m}^2 \text{ Pa}^{-1} \text{ s}^{-1}$; Young's modulus of 5.77 kPa, Poisson's ratio of 0.4879, void ratio e of 0.64 (which corresponds to a porosity of 39%) and hydraulic permeability of $\tilde{k} = 2.33 \cdot 10^{-14} \text{ m}^2 \text{ Pa}^{-1} \text{ s}^{-1}$.

Quantitative error metrics of the optimisation procedure for the proposed poroelastic model are reported in Table 2. The different components of the cost function are reported, namely J_1 (eq. 3) (peak stress error), J_2 (eq. 4) (end slope error), J_3 (eq. 5) (normalised root mean square error) and J (eq. 6) (cost function). These metrics were also assessed on the numerical curves stress-time curve fitted with the visco-hyper-elastic model in Vaidya and Wheatley [39] and reported in the table for comparison. The cost function between the optimised poroelastic numerical curve and the experimental curve is smaller with the proposed poroelastic model than with the visco-hyper-elastic model in Vaidya and Wheatley [39] (0.0016 versus 0.21 for the slow and 0.0061 versus 0.2477 for the fast).

Model	Strain-rate	J_1 (eq. 3)	J_2 (eq. 4)	J_3 (eq. 5)	J (eq. 6)
Uncoupled Yeoh/Prony visco-hyper-elastic	Slow	0.0283	0.5936	0.0081	0.21
	Fast	0.1559	0.4611	0.0046	0.2477
Poro-linear-elastic Current study	Slow	0.00005	0.00079	0.0039	0.0016
	Fast	0.0026	0.0092	0.007	0.0061

Table 2: Error metrics of the average experimental stress calibrated models for the fast and slow strain-rates of the model proposed by Vaidya and Wheatley [39] and the current study's model

3.3. One to one sample calibration

The one to one calibration was carried out on $n=15$ samples (numbered 1 to 15) for the slow strain-rate loading condition and on $n=16$ samples (numbered 16 to 31) for the fast strain-rate loading condition. The corresponding stress-time curves for each sample are reported in Figures 2 and 3 respectively for the slow and for the fast loading rates. Visually inspecting the 31 calibrated curves, it can be observed that most of the samples are not fully consolidated at the end time of the experiments as the respective slope is non-zero. The calibration procedure allowed to approximate the

271 slope between 350 s and 400 s with a poro-elastic model for all the samples
272 (important because all the samples were not necessarily fully consolidated
273 experimentally at 400 s). Also, the peak stress is mostly recovered by the
274 poroelastic model (N=25/31 for which the difference between the peak stress
275 assessed experimentally and that predicted by the simulation is lower than
276 5 %).

Solid Phase		Fluid Phase				Error Metrics			
Linear Elastic Law		Soil Grain Bulk Modulus		Darcy's Law		Fluid Bulk Modulus		Total	
E (kPa)	ν (-)	K^s (MPa)		k ($\text{m}^2 \text{Pa}^{-1} \text{s}^{-1}$)		Dynamic Viscosity (Pa s)		J (eq. 6)	
12.89 ± 11.29	0.4879	0.799		$2.09 \cdot 10^{-13} \pm 3.12 \cdot 10^{-13}$		1.0		0.0279 ± 0.0461	
20.16 ± 8.54	0.4879	0.799		$1.94 \cdot 10^{-13} \pm 5.71 \cdot 10^{-13}$		1.0		0.0523 ± 0.1094	
								0.0213 ± 0.0429	
								0.1005 ± 0.2582	
								J_1 (eq. 3)	
								0.0175 ± 0.0285	
								J_2 (eq. 4)	
								0.0470 ± 0.1244	
								J_3 (eq. 5)	
								0.0194 ± 0.0174	
								0.0181 ± 0.0188	

Table 3: Calibrated parameters and error metrics: mean and standard deviation. First line corresponds to slow-rate parameters and second line to fast-rate results

277 Table 3 provides the mean and standard deviation of the calibrated pa-
 278 rameters. The parameters obtained by calibration per sample are given Ap-
 279 pendix A. The same order of magnitude is obtained whether the strain-rate
 280 was fast or slow. The measured error metrics (eq. 6) of the calibration were
 281 respectively 0.0523 ± 0.1094 and 0.0279 ± 0.0461 (mean and standard devia-
 282 tion of all error metrics are provided Table 3). To quantify the goodness of
 283 fit, the value of the cost function value at the solution \mathbf{J}_{final}^{tot} is given for each
 284 sample in figure 4 below.

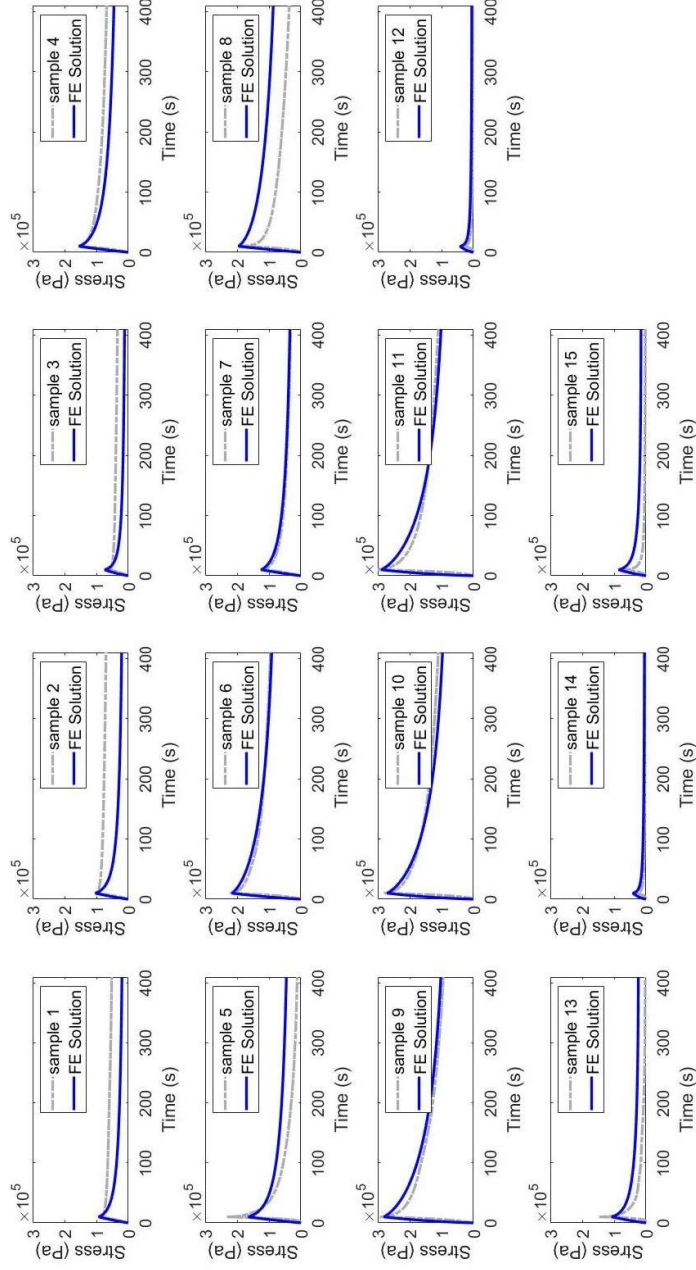


Figure 2: All 15 FE calibrated numerical solutions (blue) superimposed onto the corresponding experimental data (dashed light grey) for slow rate experiments.

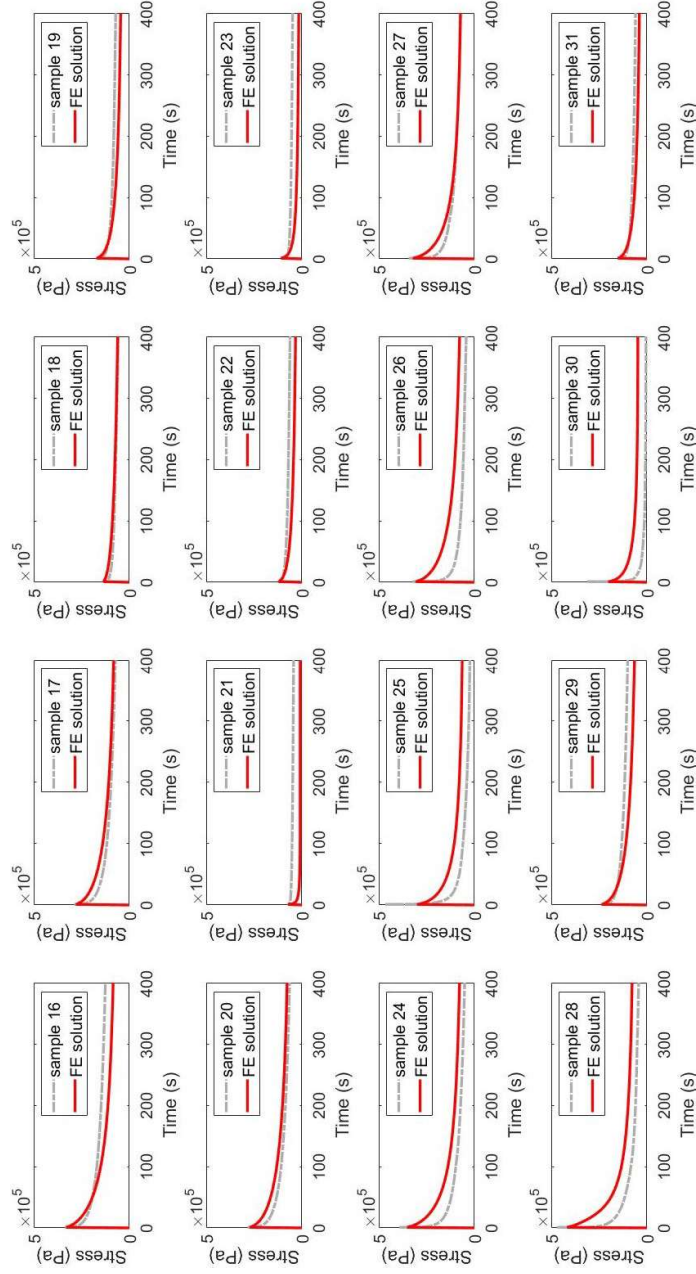


Figure 3: All 16 samples FE calibrated numerical solutions (red) superimposed onto the corresponding experimental data (dashed light grey) for fast rate experiments.

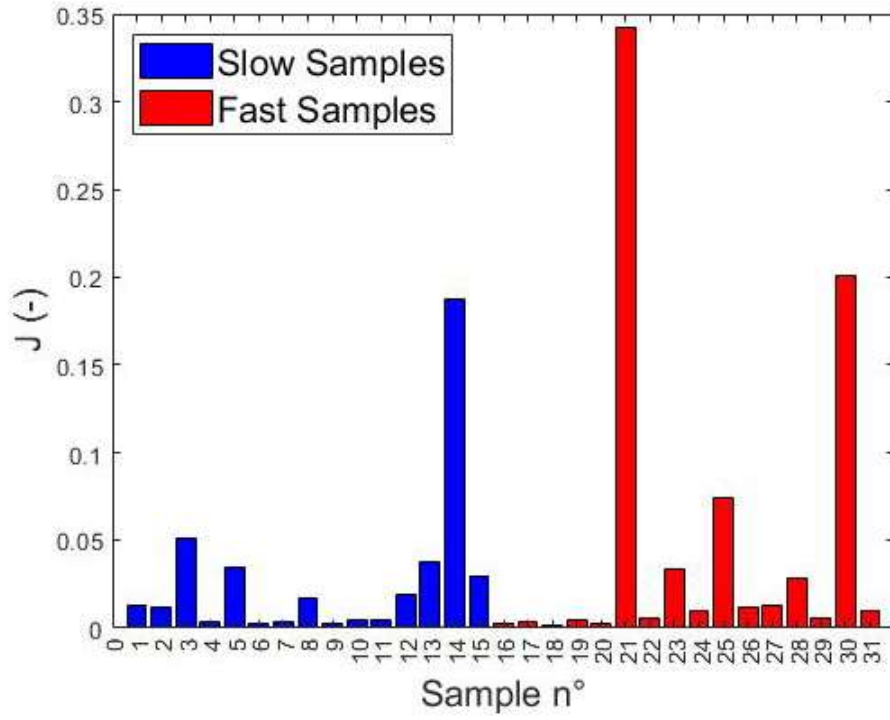


Figure 4: Cost function value at the solution for each sample. Blue corresponds to samples tested with a slow strain-rate loading and red to the samples tested with fast strain-rate loading. The proposed cost function combines the error over the peak stress, the area between the curves and the final slope (over the 50 last seconds). The cost function at the end of the identification was higher for sample 14, 21 and 30. These samples were probably already partially drained as a result of the sample preparation protocol. Hence, the assumption of full saturation might be a strong assumption.

285 4. Discussion

286 Biomechanical investigations of the time-dependent stress-strain mechan-
287 ical behaviour of skeletal muscle tissue is essential to understand and proac-
288 tively prevent Pressure Ulcer formation. Yet, in the literature, a viscoelastic
289 formulation is generally assumed for the experimental characterisation of
290 skeletal muscles, with the limitation that the underlying physical mecha-
291 nisms that give rise to the time dependent stress-strain behaviour are not
292 modelled explicitly. The objective of this study has been to explore the
293 capability of poroelasticity to reproduce the apparent viscoelastic behaviour
294 of passive muscle tissue under confined compression and to investigate the
295 contribution of extracellular fluid flow. The peak stress and consolidation
296 were recovered for most of the samples (N=25/31) by the poroelastic model
297 (normalised root-mean-square error ≤ 0.03 for fast and slow confined com-
298 pression conditions).

299 Two strong modelling assumptions have been made for drained solid
300 phase in this work: it was assumed to be both quasi-incompressible and
301 linear elastic. The assumption of a quasi-incompressible drained solid phase
302 seems reasonable because muscle fibres may exhibit nearly incompressible
303 behaviour as fluid-filled structures with no fluid transport across the cell
304 boundary. There is evidence that this is the case (Sleboda and Roberts
305 [42]) and previous modeling work of muscle tissue as a multi-phase material
306 utilized a solid phase Poisson's ratio of 0.4 (Wheatley et al. [43]). If the
307 drained solid phase was assumed to be highly compressible, this would lead
308 to a different set of calibrated constitutive poro-elastic parameters (the reader
309 is referred to appendix F) strongly suggesting that further experimental and
310 theoretical investigations are needed to shed more light on the mechanical
311 behaviour of the drained solid scaffold.

312 The assumption that a linear elastic model can be used to approximate
313 the mechanical response of the drained solid phase up to 15% of global com-
314 pression is indeed a strong one considering that many studies in the literature
315 reproduce the finite deformation of soft tissues in compression in the context
316 of Pressure Ulcer prevention using a hyper-elastic constitutive formulation
317 (Al-Dirini et al. [22], Moerman et al. [14], Oomens et al. [44], Traa et al.
318 [45], Lee et al. [46], Verver et al. [47], Levy et al. [48], Linder-Ganz et al.
319 [11], Sopher et al. [49], Zeevi et al. [50]). Yet, as demonstrated in appendix
320 E, the hyper-elastic constitutive formulations assumed in the literature gen-
321 erally result in a quasi-linear stress versus strain behaviour in compression.

These results are also consistent with the results reported in Gras et al. [51] which provides evidences that a linear elastic model can be used to correctly approximate the mechanical response of tissues in confined compression (without fluid leakage). These also suggest that the main sources of non-linearities mostly come from the geometry of the samples. The large spread of estimated values of Young's modulus obtained with two loading conditions (fast or slow rate) can most probably be explained by the ill-posed nature of the inverse problem defined in this study (there is no unique solution). Future perspective work will focus on fitting stress relaxation data of muscle in both Confined Compression and Unconfined Compression.

The strength of the poroelastic model assumed in this study is the fact that we model mechanistically the phenomenon that induce the time-dependent behavior: i.e. drainage. Also, the model has a lower number of constitutive parameters compared to more complex constitutive models employed in the literature to capture the temporal evolution of muscle tissue. For example, the visco-hyper-elastic model assumed in Vaidya and Wheatley [39] has 18 parameters to calibrate versus 6 parameters in the present study: the Young's modulus and Poisson's ratio of the drained solid matrix, the void ratio and hydraulic permeability of the sample, and the soil grain's and fluid's bulk moduli. As it was the case in most of the previous studies cited, we assessed a macroscopic quasi-incompressible behaviour for the solid scaffold with a Poisson's ratio fixed to 0.4879. The identified Young's modulus were on average of $16.63 \pm 10.48 \text{ kPa}$ (min: 2kPa; max: 31.19kPa) for both fast and slow rate experiments.

Few poroelastic models were previously proposed for the muscle - most of them used the poroelastic framework to model the mechanical behaviour of cartilage (Klika et al. [52]) and bone (Cowin [53], Hellmich and Ulm [54]). In experiments carried out over four New Zealand White Rabbits biceps femoris muscles, Wheatley et al. [55] identified a mean hydraulic permeability value of $7.41 \cdot 10^{-11} \text{ m}^2 \text{ Pa}^{-1} \text{ s}^{-1}$ with a standard error of $2.2 \cdot 10^{-11} \text{ m}^2 \text{ Pa}^{-1} \text{ s}^{-1}$. These values are higher than the calibrated values of this study (average $(2.01 \pm 4.57) \cdot 10^{-13} \text{ m}^2 \text{ Pa}^{-1} \text{ s}^{-1}$, min: $7.66 \cdot 10^{-15} \text{ m}^2 \text{ Pa}^{-1} \text{ s}^{-1}$; max: $2.40 \cdot 10^{-12} \text{ m}^2 \text{ Pa}^{-1} \text{ s}^{-1}$) but stay close in order of magnitude from the ones we found. On the contrary, Gimnich et al. [27] reported a permeability to fluid flow $\in [3.64 \cdot 10^{-14}; 1.27 \cdot 10^{-9}] \text{ m}^2 \text{ Pa}^{-1} \text{ s}^{-1}$ if a dynamic viscosity of 1Pa.s is considered.

A mean void ratio of 0.56 ± 0.3 (min: 0.092; max: 0.94) was found in this contribution. Argoubi and Shirazi-Adl [28] reported initial void ratios

360 between 0.1 and 0.3 for bones and cartilage. Our order of magnitude is
361 higher but is still under an equivalent porosity of 50% for the muscle tissue.
362 This is consistent also with the observation that skeletal muscle consists of
363 approximately 75% bound and free fluid (Sjogaard and Saltin [56]).

364 The calibrated results also showed some limitations of the poroelastic
365 model used. Indeed, the toe-region of the curve did not follow the exper-
366 imental curves as the initial slope is non-null. This could either be a con-
367 sequence of the linear constitutive models used to represent the mechanical
368 behaviour of both the solid scaffold (Hooke's law) and the fluids (Darcy's
369 law) or come from experimental uncertainties (a default of parallelism be-
370 tween the sample and the loading plate). In the second case, the interstitial
371 fluid would first have a lower impact on the measured reaction force, and the
372 toe region would change. This assumption is also supported by the results
373 of Soltz and Ateshian [57] whose experimental stress curve of the cartilage
374 with its interstitial fluid in confined compression also has a non-null initial
375 slope.

376 Although the authors had access to the experimental unconfined com-
377 pression data, the authors have not been able, in this work, to numerically
378 reproduce, in a relevant way, the boundary conditions of the experiment.
379 This is a limitation of the current work because demonstrating that the pro-
380 posed model is capable of reproducing the mechanical response of skeletal
381 muscle tissue under different loading and boundary conditions (i.e. Con-
382 fined/Unconfined Compression, slow/fast loading conditions) would further
383 establish that poro-elasticity is sufficient to capture the underlying phys-
384 ical mechanisms that give rise to the time dependent stress-strain behaviour.
385 Future work will focus on this aspect.

386 Despite the limitations of the present modelling work, this contribution
387 provides an important step toward a mechanistic interpretation of passive
388 muscle tissue undergoing compression in the context of **Deep Tissue Injury**
389 prevention. Results support the idea that the extracellular fluid contributes
390 to the apparent viscoelastic behaviour of passive muscle tissue under confined
391 compression. One main limitation of this work is the lack of experimental
392 evidences on the micro-structural organisation and composition of the sam-
393 ples (porosity, permeability). This leads to the identification of constitutive
394 parameters that are not unique and which affects the interpretation of the
395 material mechanical behaviour. Further work will focus on experimental
396 assessment of the impact of these assumptions and explore feasibility of de-
397 veloping non-invasive methods to calibrate these parameters based on in vivo

398 data.

399 Building upon recent developments on cancer modelling (Urcun et al.
400 [34], Sciumè et al. [35], Sciumè [36], Gray and Miller [37], Mascheroni et al.
401 [38]), a potential perspective work is to couple the current modelling frame-
402 work with multiphase/mutliphysics models of bio-chemical processes respon-
403 sible of the onset of **Deep Tissue Injury** initiation, and to assess the impact of
404 these parameters on the mechanical response. The interplay between chemi-
405 cal-biological-mechanical factors is key to understand and eventually predict
406 the initiation and propagation of soft tissue damage under extreme conditions
407 of deformation and ischaemia. This kind of approach could be necessary in
408 order to shed light on the relative importance (and the existence or absence of
409 coupling according to the sub-populations at risk) of the parameters proven
410 to be decisive in the development of pressure **ulcers**.

411 5. Conclusions

412 To test the hypothesis that poroelasticity is capable of reproducing the
413 apparent viscoelastic behaviour of passive muscle tissue under confined com-
414 pression, an axisymmetric Finite Element model was developed in ABAQUS.
415 For each of the N=31 cylindrical porcine samples tested under fast and slow
416 confined compression by Vaidya and collaborators, a one-to-one inverse anal-
417 ysis was performed to calibrate the specimen-specific constitutive parameters.
418 The peak stress and consolidation were recovered for most of the samples
419 (N=25) by the poroelastic model. The strength of the proposed model of
420 this study is its fewer number of variables. This contribution provides an
421 important step toward a mechanistic interpretation of passive muscle tissue
422 undergoing compression in the context of **Deep Tissue Injury** prevention.
423 Poroelasticity also represents a promising approach for integrating multi-
424 scale/multiphysics data to probe biologically relevant phenomena at a smaller
425 scale. The incorporation of poroelasticity to clinical models of **Deep Tissue**
426 **Injury** formation could lead to more precise and mechanistic explorations of
427 soft tissue injury risk factors.

428 6. Declaration of competing interest

429 Authors have no conflicts of interest to report.

430 **7. Acknowledgment**

431 The authors received no financial support for the research, authorship,
432 and/or publication of this article.

433 Appendix A. Supplementary Data

434 Supplementary data to this article (.inp ABAQUS files, pre and post
435 processing python files for ABAQUS, calibrated and raw data) can be found
436 online.

437 Appendix B. Porous medium mechanics

438 Considering its architecture, the passive muscle tissue can be considered
439 as a multi-phase tissue, composed by a solid scaffold and two liquid phases:
440 the blood contained by blood vessels and the surrounding Interstitial Fluid
441 (IF) (Sciumè [36]). With experimentation performed *ex vivo* on small sam-
442 ples, it was assumed that there was no blood and the model was based only
443 on a single level of porosity with the solid scaffold, filled with IF. Also, the
444 porous medium was assumed to be fully saturated.

445 In the remainder of the test, the following convention is assumed: \bullet^s
446 denotes the solid phase and \bullet^l denotes the fluid phase (IF). The primary
447 variables of the problem are the pressure applied in the pores of the porous
448 medium and the displacement of the solid scaffold. Then, a first relationship
449 (eq. B.1) linking the different volume fractions, can be defined. The volume
450 fraction of the phase α is defined by (eq. B.2). ε^l is also called the porosity
451 of the medium and is related to the void ratio, e , by eq. B.3.

$$\varepsilon^s + \varepsilon^l = 1 \quad (\text{B.1})$$

$$\varepsilon^\alpha = \frac{\text{Volume}^\alpha}{\text{Volume}^{total}} \quad (\text{B.2})$$

$$e = \frac{\varepsilon^l}{1 - \varepsilon^l} \quad (\text{B.3})$$

452 Assuming that there is no inter-phase mass transport, the spatial form of
453 the mass balance equation of the solid and liquid phase is respectively then
454 given by equations (eq. B.4) and (eq. B.5).

$$\frac{D^s}{Dt}(\rho^s \varepsilon^s) + \rho^s \varepsilon^s \nabla \cdot \mathbf{v}^s = 0 \quad (\text{B.4})$$

$$\frac{D^s}{Dt}(\rho^l \varepsilon^l) + \nabla \cdot (\rho^l \varepsilon^l (\mathbf{v}^l - \mathbf{v}^s)) + \rho^l \varepsilon^l \nabla \cdot \mathbf{v}^s = 0 \quad (\text{B.5})$$

455 Where $\frac{D^s}{Dt}$ is the particle derivative with respect to the movement of the phase
 456 \bullet^s , \mathbf{v}^α is the local velocity vector of the phase α and ρ^α the density of the
 457 phase α .

458 Using (eq. B.1), (eq. B.4) gives:

$$\frac{D^s}{Dt}(\rho^s(1 - \varepsilon^l)) + \rho^s(1 - \varepsilon^l)\nabla \cdot \mathbf{v}^s = 0 \quad (\text{B.6})$$

459 For the fluid phase, Darcy's law (eq. B.7) is used to evaluate the fluid
 460 flow in the porous medium.

$$\varepsilon^l(\mathbf{v}^l - \mathbf{v}^s) = -\frac{k^\varepsilon}{\mu^l}(\nabla p - \rho^l \mathbf{g}) \quad (\text{B.7})$$

461 Where k^ε is the intrinsic permeability (m^2), μ^l is the dynamic viscosity (Pa s),
 462 p the pressure and \mathbf{g} the gravity. $\frac{k^\varepsilon}{\mu^l}$ is called the hydraulic permeability.

463 Then, (eq. B.7) is injected in (eq. B.5) as follows:

$$\frac{D^s}{Dt}(\rho^l \varepsilon^l) - \nabla \cdot (\rho^l (\frac{k^\varepsilon}{\mu^l}(\nabla p - \rho^l \mathbf{g}))) + \rho^l \varepsilon^l \nabla \cdot \mathbf{v}^s = 0 \quad (\text{B.8})$$

$$\iff \frac{D^s}{Dt}(\rho^l \varepsilon^l) - \nabla \cdot (\rho^l (\nabla (\frac{k^\varepsilon}{\mu^l} p))) + \nabla \cdot (\rho^l \frac{k^\varepsilon}{\mu^l} \mathbf{g}) + \rho^l \varepsilon^l \nabla \cdot \mathbf{v}^s = 0 \quad (\text{B.9})$$

464 Concerning the mechanical constitutive model, similarly to what was pro-
 465 posed by Terzaghi for a 1D consolidation (Appendix C.1), an effective stress
 466 tensor denoted \mathbf{t}^{eff} is responsible for all deformation of the solid ECM scaf-
 467 fold. Hence the total stress tensor is defined by (eq. B.10).

$$\mathbf{t}^{tot} = \mathbf{t}^{eff} - \beta p \mathbf{I}_d \quad (\text{B.10})$$

468 Where β is the Biot's coefficient and \mathbf{I}_d is the identity matrix.

469 Assuming linear elastic behaviour, the effective stress tensor is defined by
 470 (eq. B.11).

$$\mathbf{t}^{eff} = \mathbf{C} : \mathbf{d} \quad (\text{B.11})$$

471 Then, applying the conservation of momentum, the governing equations
472 of this one level porous medium are:

$$\frac{D^s}{Dt}(\rho^s(1 - \varepsilon^l)) + \rho^s(1 - \varepsilon^l)\nabla \cdot \mathbf{v}^s = 0 \quad (\text{B.12})$$

$$\frac{D^s}{Dt}(\rho^l \varepsilon^l) - \nabla \cdot \rho^l (\nabla (\frac{k^\varepsilon}{\mu^l} \mathbf{p})) + \nabla \cdot (\rho^l \frac{k^\varepsilon}{\mu^l} \mathbf{g}) + \rho^l \varepsilon^l \nabla \cdot \mathbf{v}^s = 0 \quad (\text{B.13})$$

$$\nabla \cdot (\mathbf{t}^{tot}) + f_v = \rho^s \gamma^s \quad (\text{B.14})$$

473 Where f_v are the force densities applied to the medium and γ^s is the acceleration of the
474 solid phase.

475 Three boundaries were defined: the first one, Ω_u has imposed displace-
476 ment (eq. B.15), the second one Ω_s has imposed external forces (eq. B.16)
477 and Ω_p is submitted to an imposed pressure (fluid leakage condition (eq.
478 B.17)). We obtain:

$$\mathbf{t}^{eff} = \mathbf{t}^{imposed} \text{ on } \Omega_s \quad (\text{B.15})$$

$$\mathbf{u}^s = \mathbf{u}^{imposed} \text{ on } \Omega_u \quad (\text{B.16})$$

$$p = 0 \text{ on } \Omega_p \quad (\text{B.17})$$

479 **Appendix C. Poroelasticity to capture the time-dependent response** 480 **of muscle**

481 Most of biological soft tissues has a porous/fibrous nature consisting of a
482 solid scaffold giving mechanical stability and one or more fluid or pseudo-fluid
483 phases which saturate the porosity. Hence, to mechanistically model a bio-
484 logical human (or animal) tissue accounting for the interaction between the
485 solid matrix (primarily constituted by proteins and collagen fibers) and the
486 fluid phases one must use porous media mechanics. Despite this conscious-
487 ness, researchers are still today much more used to employ viscoelasticity to
488 model the time-dependent behavior of soft tissues. If on one hand its is true
489 that viscoelastic models are typically very effective to fit usual experimental
490 tests, however the underlying physical mechanisms that give rise to the time-
491 stress dependent behavior is not well known and found material parameters
492 may vary with the considered boundary conditions.

493 Lets we consider two reference models: i) a two-phase (one solid-one fluid)
494 poroelastic model and ii) a rheological viscoelastic model constituted by a

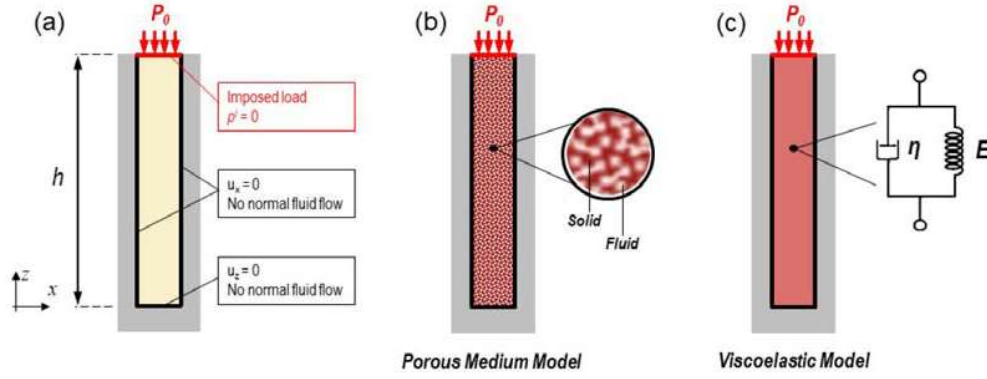


Figure C.5: One dimensional consolidation. (a) Geometry and boundary conditions; (b-c) porous medium and viscoelastic models

495 Kelvin-Voight chain; and use these two models to simulate a 1D confined
 496 compression test. In this test the tissue is constrained in a cylindrical or
 497 prismatic chamber and compressed at the top surface with a constant pres-
 498 sure, p_0 . The specimen is fully sealed with the exception of the top surface
 499 where a porous membrane allows drainage of the inside fluid during the test.
 500 The geometry and boundary conditions of the test are represented in Figure
 501 C.5. This kind of test, which takes up the paradigms of one of the most im-
 502 portant characterization essay in soil mechanics (it is named oedometer test
 503 or 1D consolidation test), is a very frequent test performed to characterize
 504 the dynamics response of biological soft tissue.

505 *Appendix C.1. Terzaghi's analytic solution*

506 The Terzaghi analytical solution given by (eq. C.1) gives the solution
 507 to 1D porous medium mechanics a series expansion function of the 1D-
 508 coordinate. Hereunder are recalled the hypotheses of the Terzaghi's solu-
 509 tion (Tavenas, F. et al. [58]):

- 510 1. the sample is submitted to small and unidirectional strains
- 511 2. The solid grains and fluid are supposed in-compressible
- 512 3. The material is homogeneous
- 513 4. The mechanical parameters stay constant during all the settlement
- 514 5. The fluid leakage is unidirectional and follows the Darcy's law

- 515 6. There is a linear law between the effective stresses and volume variation
 516 of the soil
 517 7. The soil has no structural viscosity or secondary settlement

$$p = \frac{4p_0}{\pi} \sum_{k=1}^{+\infty} \frac{(-1)^{k-1}}{2k-1} \cos[(2k-1)\frac{\pi}{2}\frac{z}{h}] \exp[-(2k-1)^2 \frac{\pi^2}{4} \frac{c_v t}{h^2}] \quad (C.1)$$

$$c_v = \frac{k^\varepsilon}{\mu^l (S + \frac{\beta^2}{M})} \quad (C.2)$$

$$M = \frac{3K^s(1-\nu)}{(1+\nu)} \quad (C.3)$$

$$S = \frac{\beta - \varepsilon_0^l}{K^s} + \frac{\varepsilon_0^l}{K^l} \quad (C.4)$$

518 Where p_0 is the full applied load, z is the altitude, h is the initial height of the sample ,
 519 c_v is the consolidation coefficient defined by (eq. C.2), M the longitudinal modulus (eq.
 520 C.3), K^α the bulk's modulus of the α phase, ν the Poisson's ratio, S the inverse of the
 521 Biot Modulus (eq. C.4), β is the Biot coefficient and ε_0^l is the initial porosity.

522 Looking to (eq. C.1), a consolidation time $T_v = \frac{h^2}{c_v}$ was defined. Ususally,
 523 in the assumption of a compressibility of the phases larger than the porous
 524 medium compressibility, then $\beta = 1$ and $S = 0$ gives:

$$c_v = \frac{k^\varepsilon M}{\mu^l} \quad (C.5)$$

$$T_v = \frac{h^2 \mu^l}{k^\varepsilon M} \quad (C.6)$$

525 The consolidated stress, $t^{consolidated}$ was also computable (eq. C.7),

$$t^{consolidated} = M \frac{u_{imposed}}{h} \quad (C.7)$$

526 Where $u_{imposed}$ is the imposed displacement on the top surface and h is the initial height
 527 of the sample.

528 So in this minimal version of porous medium model the behaviour is gov-
 529 erned by three parameters: the elastic coefficients E and ν (which determine

530 M) and the ratio between the intrinsic permeability of the solid and the dy-
 531 namic viscosity of the fluid $\frac{k}{\mu^l}$. From eq. C.1 quasi-analytical solutions can
 532 be derived for the vertical strain and vertical displacement along the vertical
 533 coordinate.

534 *Appendix C.2. Viscoelastic formulation*

535 The analytical solution of the viscoelastic model has a much simpler form
 536 and gives the vertical displacement of the points along the vertical coordinate
 537 of the column as a function of time

$$u_z(z, t) = -\frac{p_0 t}{M} \left[1 - \frac{E t}{\eta} \right] \quad (\text{C.8})$$

538 So also in this model the behaviour is governed by three parameters: the
 539 elastic coefficients E (stiffness of the spring in the 1D rheological model) and
 540 ν and the viscosity of the damper η .

541 *Appendix C.3. Comparison between the two solutions*

542 For the simulated experiment the column height, h is of 1 cm and the
 543 pressure, p_0 , imposed at the top of the column is equal to 10 Pa. For the
 544 porous medium formulation the following parameters are assumed: Young's
 545 modulus E equal to 1 kPa; Poisson's ration ν equal to 0.4; intrinsic perme-
 546 ability of the solid scaffold, k , equal to $4 \times 10^{-16} \text{ m}^2$; and dynamic viscosity
 547 of the fluid, μ^l , equal to 0.001 Pa.s. For the viscoelastic model the Young's
 548 modulus and the Poisson's ratio have the same values of the porous medium
 549 model. For the viscosity of the damper, η , a value of $4.4 \times 10^7 \text{ Pa.s}$ has been
 550 identified which, for h equal to 1 cm, gives an overall response in term of ver-
 551 tical displacement of the top point very similar to that of the porous medium
 552 model (see Figure C.6.d solid lines). In this figure we can observe that the
 553 initial agreement between the two formulations is not optimal; however, after
 554 24 hours the two curves are superposed. To better understand the behaviour
 555 of the two models we can analyse more in depth such results by plotting the
 556 vertical displacement along the vertical coordinate at different times for the
 557 porous medium and the viscoelastic models. In Figure C.6.c we can observe
 558 that in the porous medium model the displacement in proximity of the drying
 559 surface grows initially more rapidly than in the viscoelastic case since this
 560 area is rapidly consolidated in the first phase of the compression process.
 561 This can be more easily understood looking at Figure C.6.b which shows the
 562 fluid pressure along the vertical coordinate at different times for the porous

medium model. We can observe that the pressure decreases progressively over the time due to the consolidation process.

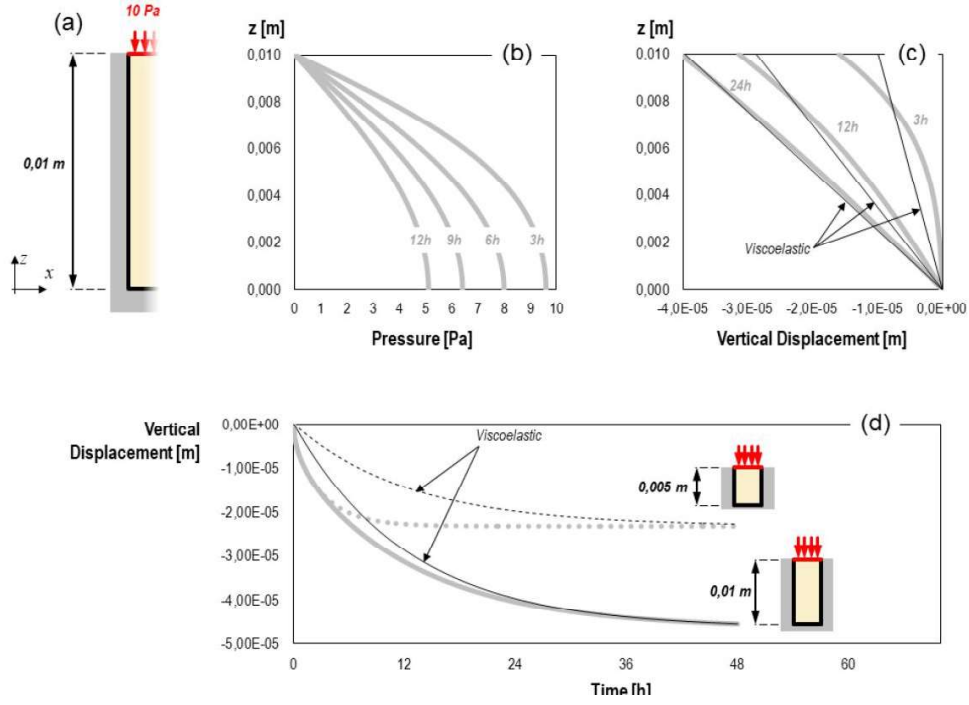


Figure C.6: Results for the 1D consolidation case. (a) Specimen geometry. (b) Fluid pressure along the vertical coordinate at different times (porous medium model). (c) Vertical displacement along the vertical coordinate at different times for the porous medium model (gray line) and the viscoelastic model (black line). (d) Vertical displacement of the top surface versus time for the porous medium model (gray line) and the viscoelastic model (black line); two cases are considered: $h = 1$ cm (solid lines) and $h = 0.5$ cm (dashed lines).

Hence, this initial heterogeneity of strain along the vertical coordinated cannot be reproduced with the viscoelastic model since the drainage of the fluid is not explicitly modelled. However, the worst is still to come. Let's we consider now a column with h equal to 0.5 cm, one half of the previously assumed height. The overall vertical displacement of the top surface is depicted in Figure C.6.d. for the porous medium (gray dashed line) and viscoelastic (black dashed line) models. The figure shows that this time the dynamics is fully different. In the porous medium case the column consolidates much faster than in the viscoelastic case. If we compare the solution

of $h = 0.5$ cm (dashed lines) with those of $h = 1$ cm (solid lines) we see that the dynamics of the viscoelastic model remains the same (obviously with a different asymptotic tendency) while the porous medium model consolidates almost four time faster for $h = 0.5$ cm. To decipher the reason of the discordance between solutions of the viscoelastic and porous medium models one can consider the unit of the factors that drive time dependent response in the two cases. Looking firstly at the analytical solution of the viscoelastic model from eq. C.8 we deduce that the characteristic time of the consolidation process is proportional to $\frac{\eta}{E}$ (that quantity has the dimension of a time). In the porous medium model the time dependent response is governed by the consolidation coefficient and the characteristic time of the consolidation process is proportional to $\frac{h^2}{c_v}$ (eq. C.6) and that therefore the length of the drainage path h has a capital impact on the consolidation dynamics. From these analyses we deduce that for the porous medium model once parameter are identified these remain suitable also in other experimental situations. Conversely, if we want to mimic the behaviour of a porous material with a viscoelastic model we must adjust the parameter η accounting for the specimen size and boundary conditions. If on one hand this is feasible for a 1D case, on the other hand we can imagine that could be very difficult for more complex configurations.

Appendix D. Terzaghi's analytic solution with Abaqus

For the confined compression tests, the expected result was similar to a 1D compression. Hence, the Terzaghi analytical solution given by (eq. C.1) was used to assess the reliability of the ABAQUS model considered. The analytical solution is recalled section Appendix C.1.

Solid Phase			Fluid Phase			
Linear Elastic Law		Soil Grain Bulk Modulus	Darcy's Law			Fluid Bulk Modulus
E (kPa)	ν (-)	K^s (MPa)	k ($\text{m}^2 \text{Pa}^{-1} \text{s}^{-1}$)	Dynamic Viscosity (Pa.s)	Void ratio (-)	K^f (MPa)
1.0	0.4	0.001 (full line) / 2200 (dashed line)	$4 \cdot 10^{-13}$	1.0	1.0	2200

Table D.4: Parameters used in the verification model

According to section 2.2, a preliminary study was carried out over a small strain model. A 2D axi-symmetric ABAQUS model composed of (n=60 CAX4PH elements) of an imposed load experiment was proposed. An imposed pressure of 10 Pa was applied on the top surface and boundary conditions are presented Figure C.5. The material parameters are given Table D.4. Two different conditions were tested: $K^s = 0.001 \text{MPa} \implies \beta =$

605 $1 - \frac{E}{3K^s(1-2\nu)} = 0.83$ which is lower than the soil bulk modulus expected for
 606 the muscle and $K^s = 2.2e9\text{MPa} \Rightarrow \beta = 1 - \frac{E}{3K^s(1-2\nu)} \approx 1.0$ which allowed
 607 to be closer to the assumption 2 above.

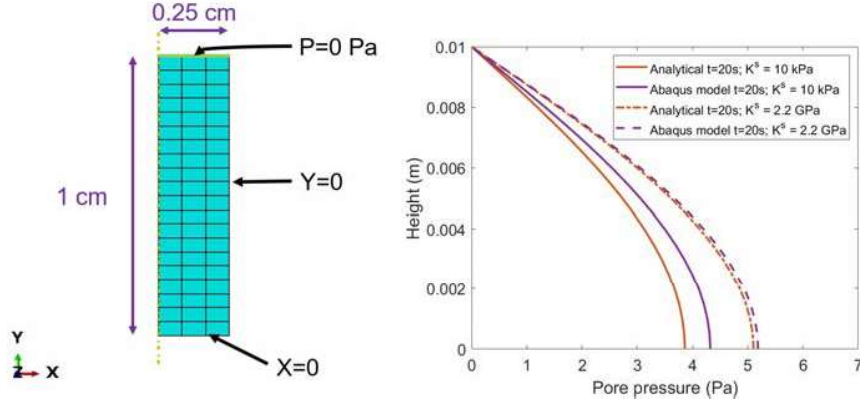


Figure D.7: Discretized Finite Element model (left) and comparison to the analytical solution (right)

608 The result obtained are presented on the right of Figure D.7. The dashed
 609 curves correspond to the quasi-incompressible soil grains and plain curves to
 610 the non-incompressible soil grain model. As expected, the quasi-incompressible
 611 soil grains' curve was quasi-super-imposed. There was a difference for the
 612 non-incompressible soil grain, probably because the hypotheses were not fully
 613 covered but the order of magnitude was good.

614 Finally, as our samples were submitted to high strains, the use of the anal-
 615 itycal solution was not possible to directly model the available experimental
 616 data.

617 Appendix E. Hyper-elasticity models for the buttock tissue

618 To quantitatively assess the influence of the assumed constitutive law
 619 when simulating the finite deformation of soft tissue in compression in the
 620 context of Pressure Ulcer prevention, a the semi-confined compression exper-
 621 iment is simulated (Figure E.8 below). The numerical experiment consists in
 622 testing in compression a cylindrical specimen with low-aspect ratio. In the
 623 semi-confined configuration, the top and bottom faces of the specimen are
 624 rigidly attached to the platens of the stress-strain machine to ensure no-slip
 625 boundary conditions.

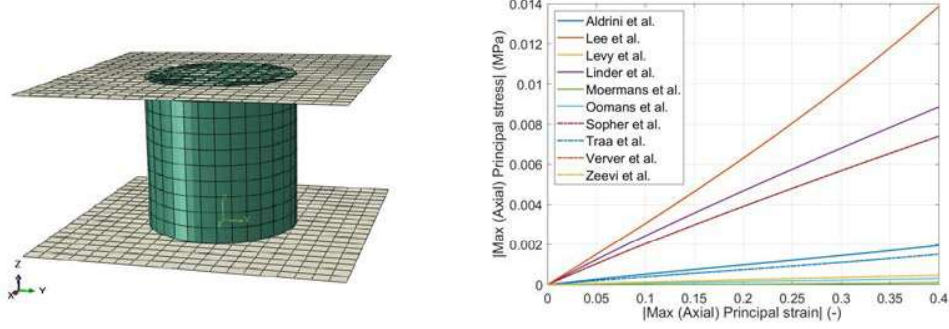


Figure E.8: Numerical model of the semi-confined experiment proposed (left) and resulting stress-strain curves (right). The references of the legend correspond to the ones of Table E.5

The constitutive laws found in the litterature are mostly variation around three main strain-energy density functions : Ogden Law (E.1), Mooney-Rivlin and Neo-Hookean (E.3). The Mooney-Rivlin is computed in abaqus as a generalized Rivlin model with one mode (E.2). For each equation, W is the strain energy density function, $\bar{\lambda}_i$ are the deviatoric stretches, \bar{I}_i are the deviatoric invariants of the Green-Cauchy left transformation tensor and J the Jacobian of the transformation tensor.

$$W(\bar{\lambda}_i) = \frac{\mu_1}{\alpha_1} \left(\sum_i \bar{\lambda}_i^{\alpha_1} - 3 \right) + \frac{1}{D_1} (J - 1)^2 \quad (\text{E.1})$$

$$W(\bar{I}_i) = C_{10}(\bar{I}_1 - 3) + C_{01}(\bar{I}_2 - 3) + \frac{1}{D_1} (J - 1)^2 \quad (\text{E.2})$$

$$W(\bar{I}_i) = C_{10}(\bar{I}_1 - 3) + \frac{1}{D_1} (J - 1)^2 \quad (\text{E.3})$$

Some articles used different forms of those equations but due to the assumption of incompressibility, all those writings are equivalent. We computed the equivalent parameters to be used in ABAQUS. The table E.5 presents for each article the considered constitutive law and the parameters used in ABAQUS. As ABAQUS uses pre-encoded equation, the parameters or the equation formulation can be simplified or slightly modified in regard of the one used in the articles.

Looking to Figure E.8, the hyper-elastic laws with their associated parameters for muscle tissue may be, at least during the 15 first percent of

compression, approximated by a linear-elastic law for the solid scaffold.

Appendix F. Poroelastic model parameter identification assuming a highly compressible drained solid phase (Poisson's ratio of 0.2)

Appendix F.1. Calibration of the average experimental relaxation curve

Similarly to the previous section, the result of the calibration of the average relaxation stress-time curve is superimposed in Figure F.9 onto the average experimental sample stress-time curve and the experimental corridor. The calibrated visco-hyper-elastic numerical model reported in Vaidya and Wheatley [39] is also superimposed for the ease of comparison.

The parameters identified were, respectively, for fast and slow strain-rate: Young's modulus of 149 kPa, Poisson's ratio of 0.2, void ratio e of 1.0 (which corresponds to a porosity of 50%) and hydraulic permeability of $k = 2.32 \cdot 10^{-14} \text{ m}^2 \text{ Pa}^{-1} \text{ s}^{-1}$; Young's modulus of 99.3 kPa, Poisson's ratio of 0.2, void ratio e of 0.72 (which corresponds to a porosity of 42%) and hydraulic permeability of $k = 4.16 \cdot 10^{-14} \text{ m}^2 \text{ Pa}^{-1} \text{ s}^{-1}$.

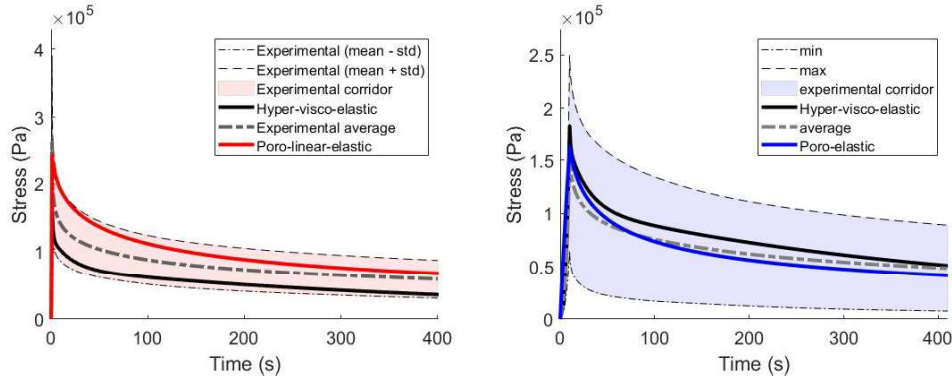


Figure F.9: Results for the fast strain-rate (left) and for the slow strain-rate (right) average experimental relaxation curve calibration. The experimental corridor of the campaign of Vaidya and Wheatley [39] is light red for the fast strain rate and light blue for the slow one, the average experimental stress is in dashed grey. The visco-hyper-elastic model calibrated in Vaidya and Wheatley [39] is in black while poroelastic model predictions with a Poisson's ratio of 0.2 are in red for the fast strain rate and blue for the slow strain-rate.

Quantitative error metrics of the optimisation procedure for the proposed poro-linear-elastic model are reported in Table F.6. The different components

660 of the cost function are the same than section 3. These metrics were also
661 assessed on the numerical curves stress-time curve fitted with the visco-hyper-
662 elastic model in Vaidya and Wheatley [39] and reported in the table for
663 the sake comparison. The cost function between the optimised poroelastic
664 numerical curve and the experimental curve is smaller with the proposed
665 poroelastic model than with the visco-hyper-elastic model in Vaidya and
666 Wheatley [39] (0.0022 versus 0.21 for the slow and 0.0375 versus 0.2477 for
667 the fast).

668 *Appendix F.1.1. One to one sample calibration*

669 The one to one calibration was carried out on the n=16 samples for fast
670 strain-rate and n=15 samples for slow strain-rate. The corresponding stress-
671 time curves for each sample are reported in Figures F.10 and F.11 respectively
672 for the slow and for the fast loading rates. Looking to the 31 calibrated
673 curves, the slope between 350 s and 400 s is mostly approximated: most of
674 the samples are not fully consolidated at the end time of the experiments
675 as the slope is non-null. Also the peak stress is mostly recovered by the
676 poroelastic model.

Article	Constitutive Law	ABAQUS Parameters
Al-Dirini et al. [22]	Ogden	$\mu_1 = 1.91e - 3\text{MPa}$ $\alpha_1 = 4.6$ $D_1 = 9.179\text{MPa}^{-1}$
Lee et al. [46]	Moonley-Rivlin	$C_{01} = 1.65e - 3\text{MPa}$ $C_{10} = 3.35e - 3\text{MPa}$ $D_1 = 4.03\text{MPa}^{-1}$
Levy et al. [48]	Neo-Hookean	$D_1 = 2.83\text{MPa}^{-1}$ $C_{10} = 3.55e - 3\text{MPa}$
Linder-Ganz et al. [11]	Neo-Hookean	$D_1 = 1.18\text{MPa}^{-1}$ $C_{10} = 4.25e - 3\text{MPa}$
Moerman et al. [14]	Ogden	$\mu_1 = 5.575e - 4\text{MPa}$ $\alpha_1 = 12$ $D_1 = 7.47\text{MPa}^{-1}$
Oomens et al. [44]	Ogden	$\mu_1 = 3.0e - 4\text{MPa}$ $\alpha_1 = 5$ $D_1 = 13.36\text{MPa}^{-1}$
Sopher et al. [49]	Neo-Hookean	$D_1 = 2.817\text{MPa}^{-1}$ $C_{10} = 3.55e - 3\text{MPa}$
Traa et al. [45]	Ogden	$\mu_1 = 1.49e - 3\text{MPa}$ $\alpha_1 = 5$ $D_1 = 57\text{MPa}^{-1}$
Verver et al. [47]	Moonley-Rivlin	$C_{01} = 1.65e - 3\text{MPa}$ $C_{10} = 3.35e - 3\text{MPa}$ $D_1 = 5.04\text{MPa}^{-1}$
Zeevi et al. [50]	Neo-Hookean	$D_1 = 53.3\text{MPa}^{-1}$ $C_{10} = 2.25e - 3\text{MPa}$

Table E.5: Table gathering all the considered articles and their associated parameters used in ABAQUS

Model	Strain-rate	J_1 (eq. 3)	J_2 (eq. 4)	J_3 (eq. 5)	J (eq. 6)
Uncoupled Yeoh/Prony visco-hyper-elastic	Slow	0.0283	0.5936	0.0081	0.21
	Fast	0.1559	0.4611	0.0046	0.2477
Poro-linear-elastic Current study	Slow	0.0014	0.00055	0.0046	0.0022
	Fast	0.0056	0.0974	0.0093	0.0375

Table F.6: Error metrics of the average experimental stress calibrated models for the fast and slow strain-rates of the model proposed by Vaidya and Wheatley [39] and the current study's model

Solid Phase		Fluid Phase			Error Metrics		
Linear Elastic Law		Soil Grain Bulk Modulus		Fluid Bulk Modulus		Peak Stress	
E (kPa)	ν (-)	K^s (MPa)		Void ratio (-)		Total	
116.02 \pm 31.89	0.2	0.799		0.81 \pm 0.24		J (eq. 6)	
133.75 \pm 24.54	0.2	0.799		1.0		0.121 \pm 0.161	
				1.0		0.12 \pm 0.13	
						J ₁ (eq. 3)	
						0.0167 \pm 0.0228	
						0.069 \pm 0.086	
						J ₂ (eq. 4)	
						0.322 \pm 0.472	
						J ₃ (eq. 5)	
						0.024 \pm 0.022	
						0.422 \pm 0.269	
						0.016 \pm 0.0105	

Table F.7: Calibrated parameters and error metrics: mean and standard deviation. First line corresponds to slow-rate parameters and second line to fast-rate results

677 Table F.7 provides the mean and standard deviation of the calibrated
678 parameters. The same order of magnitude is obtained whether the strain-
679 rate was fast or slow. The measured error metrics of the calibration were
680 respectively 0.12 ± 0.13 and 0.121 ± 0.161 (mean and standard deviation of
681 all error metrics are provided Table F.7). Once again, these results support
682 the apparent capacity of the model to mostly capture the peak stress and
683 relaxation described previously also minimising the root mean square error
684 metric.

685 To quantify the goodness of fit, the value of the cost function value at
686 the solution \mathbf{J}_{final}^{tot} is given for each sample in figure F.12 below.

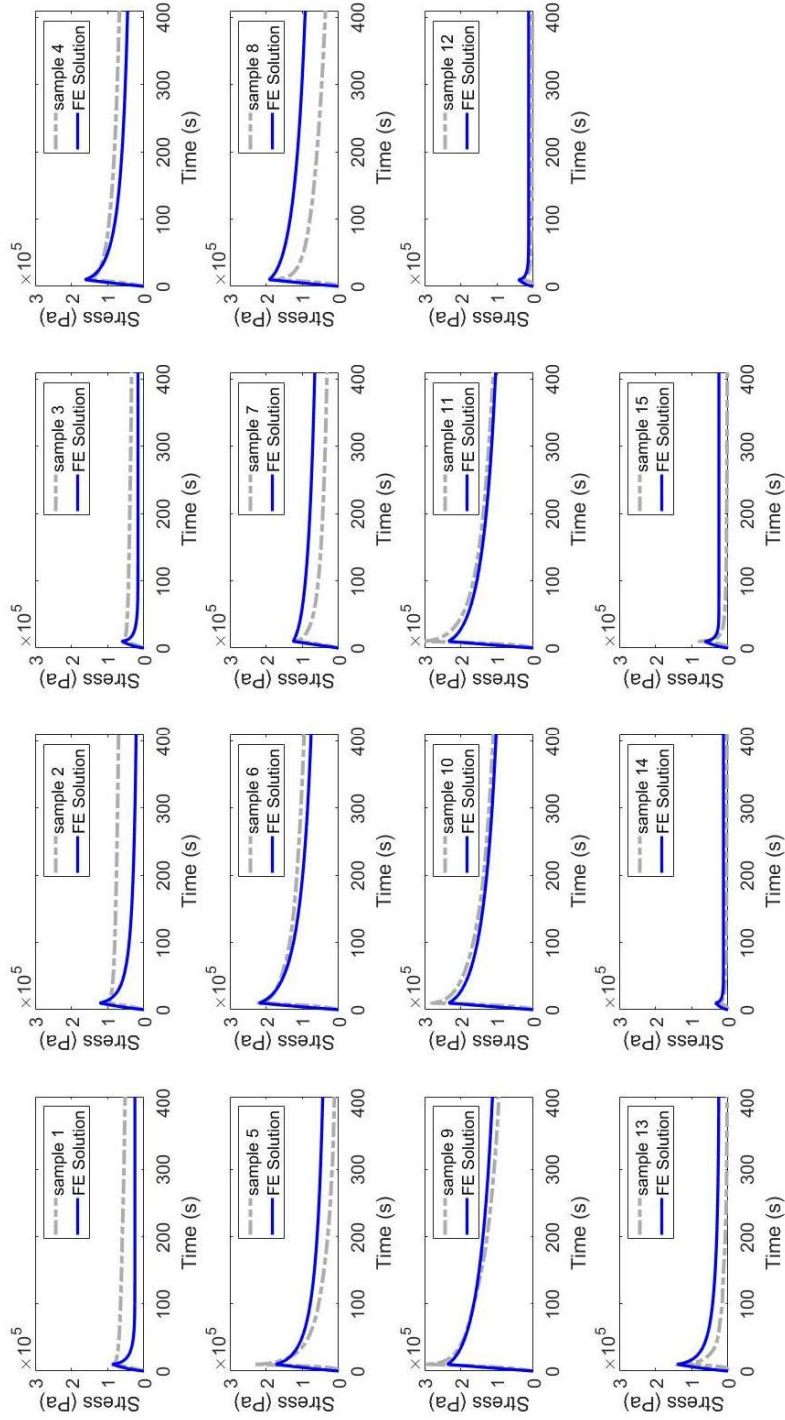


Figure F.10: All 15 FE samples calibrated models (blue) superimposed with the corresponding experimental data (light grey) for slow rate experiment

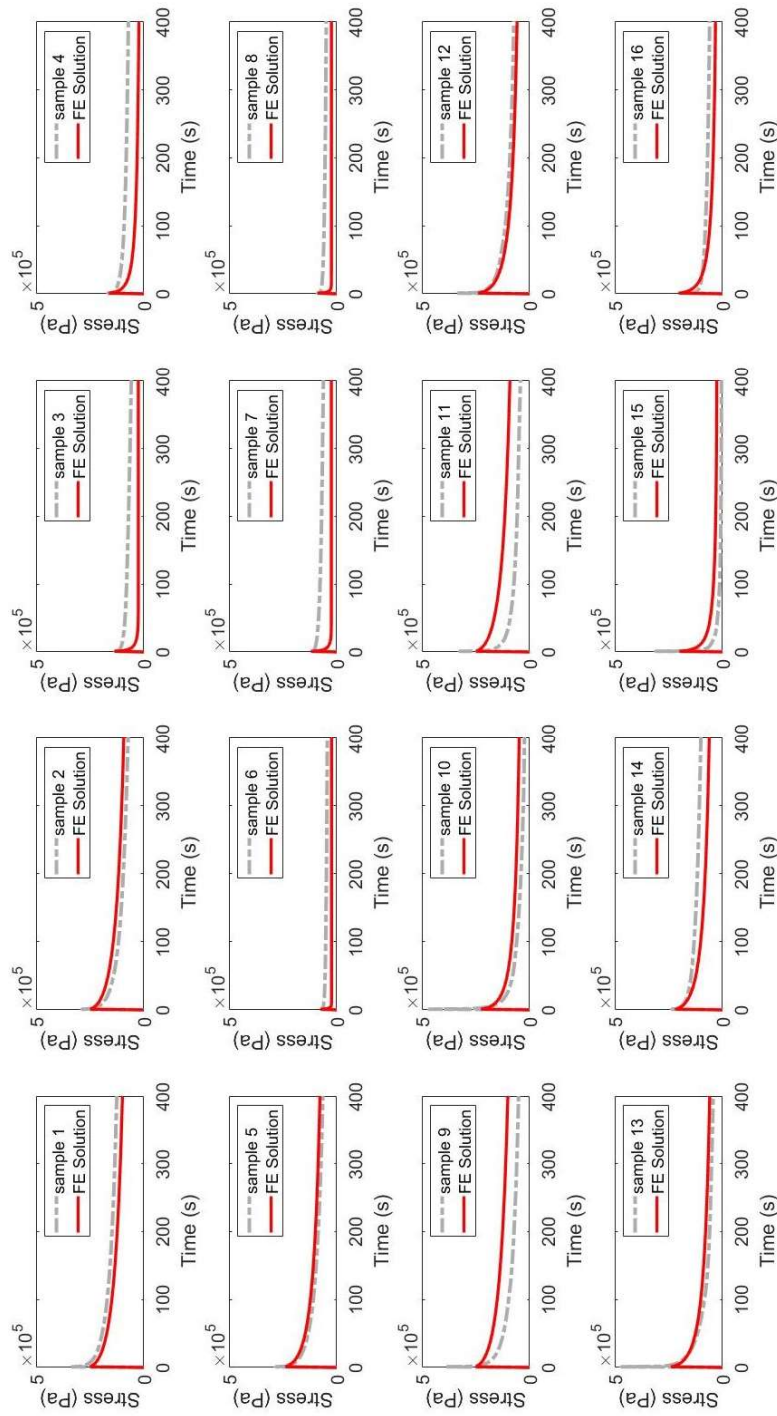


Figure F.11: All 16 samples FE calibrated models (red) superimposed with the corresponding experimental data (light grey) for fast rate experiment

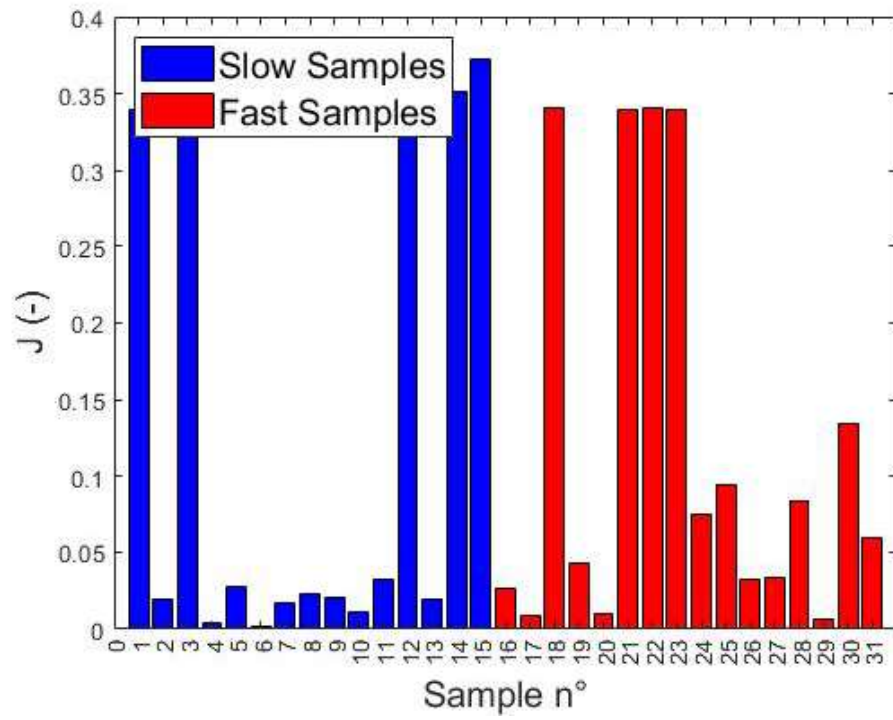


Figure F.12: Cost function value at the solution for each sample. Blue corresponds to samples tested with a slow strain-rate loading and red to the samples tested with fast strain-rate loading.

687 References

- 688 [1] A. Gefen, D. M. Brienza, J. Cuddigan, E. Haesler, J. Kottner,
689 Our contemporary understanding of the aetiology of pressure ul-
690 cers/pressure injuries, *International Wound Journal* n/a (2021). URL:
691 <https://onlinelibrary.wiley.com/doi/abs/10.1111/iwj.13667>.
692 doi:<https://doi.org/10.1111/iwj.13667>.
- 693 [2] A. Gefen, P. Alves, G. Ciprandi, F. Coyer, C. T. Milne, K. Ousey,
694 N. Ohura, N. Waters, P. Worsley, J. Black, M. Barakat-Johnson,
695 D. Beeckman, J. Fletcher, H. Kirkland-Kyhn, N. A. Lahmann,
696 Z. Moore, Y. Payan, A.-B. Schlüer, Device-related pressure ul-
697 cers: SECURE prevention, *Journal of Wound Care* 29 (2020)
698 S1–S52. URL: <https://doi.org/10.12968/jowc.2020.29.sup2a.s1>.
699 doi:10.12968/jowc.2020.29.sup2a.s1.
- 700 [3] G. Bennett, C. Dealey, J. Posnett, The cost of pres-
701 sure ulcers in the UK, *Age and Ageing* 33 (2004)
702 230–235. URL: <https://doi.org/10.1093/ageing/afh086>.
703 doi:10.1093/ageing/afh086. arXiv:<https://academic.oup.com/ageing/article-pdf/33/3/>
- 704 [4] K. Ceelen, A. Stekelenburg, S. Loerakker, G. Strijk-
705 ers, D. Bader, K. Nicolay, F. Baaijens, C. Oomens,
706 Compression-induced damage and internal tissue strains are
707 related, *Journal of Biomechanics* 41 (2008) 3399–3404.
708 URL: <https://doi.org/10.1016/j.jbiomech.2008.09.016>.
709 doi:10.1016/j.jbiomech.2008.09.016.
- 710 [5] S. Loerakker, E. Manders, G. J. Strijkers, K. Nicolay, F. P. T. Baai-
711 jens, D. L. Bader, C. W. J. Oomens, The effects of deformation, is-
712 chemia, and reperfusion on the development of muscle damage during
713 prolonged loading, *Journal of Applied Physiology* 111 (2011) 1168–
714 1177. URL: <https://doi.org/10.1152/japplphysiol.00389.2011>.
715 doi:10.1152/japplphysiol.00389.2011.
- 716 [6] A. Stekelenburg, C. W. J. Oomens, G. J. Strijkers, K. Nico-
717 lay, D. L. Bader, Compression-induced deep tissue in-
718 jury examined with magnetic resonance imaging and histol-
719 ogy, *Journal of Applied Physiology* 100 (2006) 1946–1954.

- 720 URL: <https://doi.org/10.1152/japplphysiol.00889.2005>.
721 doi:10.1152/japplphysiol.00889.2005.
- 722 [7] B. J. van Nierop, A. Stekelenburg, S. Loerakker, C. W. Oomens,
723 D. Bader, G. J. Strijkers, K. Nicolay, Diffusion of water in
724 skeletal muscle tissue is not influenced by compression in a rat
725 model of deep tissue injury, *Journal of Biomechanics* 43 (2010)
726 570–575. URL: <https://doi.org/10.1016/j.jbiomech.2009.07.043>.
727 doi:10.1016/j.jbiomech.2009.07.043.
- 728 [8] W. A. Traa, M. C. van Turnhout, J. L. Nelissen, G. J. Stri-
729 jkers, D. L. Bader, C. W. Oomens, There is an indi-
730 vidual tolerance to mechanical loading in compression induced
731 deep tissue injury, *Clinical Biomechanics* 63 (2019) 153–
732 160. URL: <https://doi.org/10.1016/j.clinbiomech.2019.02.015>.
733 doi:10.1016/j.clinbiomech.2019.02.015.
- 734 [9] S. Loerakker, A. Stekelenburg, G. J. Strijkers, J. J. M. Rijpkema, F. P. T.
735 Baaijens, D. L. Bader, K. Nicolay, C. W. J. Oomens, Temporal effects of
736 mechanical loading on deformation-induced damage in skeletal muscle
737 tissue, *Annals of Biomedical Engineering* 38 (2010) 2577–2587. URL:
738 <https://doi.org/10.1007/s10439-010-0002-x>. doi:10.1007/s10439-
739 010-0002-x.
- 740 [10] E. Linder-Ganz, G. Yarnitzky, Z. Yizhar, I. Siev-Ner, A. Gefen, Real-
741 time finite element monitoring of sub-dermal tissue stresses in indi-
742 viduals with spinal cord injury: Toward prevention of pressure ul-
743 cers, *Annals of Biomedical Engineering* 37 (2008) 387–400. URL:
744 <https://doi.org/10.1007/s10439-008-9607-8>. doi:10.1007/s10439-
745 008-9607-8.
- 746 [11] E. Linder-Ganz, N. Shabshin, Y. Itzhak, A. Gefen, As-
747 sessment of mechanical conditions in sub-dermal tissues dur-
748 ing sitting: A combined experimental-MRI and finite element
749 approach, *Journal of Biomechanics* 40 (2007) 1443–1454.
750 URL: <https://doi.org/10.1016/j.jbiomech.2006.06.020>.
751 doi:10.1016/j.jbiomech.2006.06.020.
- 752 [12] E. Linder-Ganz, S. Engelberg, M. Scheinowitz, A. Gefen, Pressure–time
753 cell death threshold for albino rat skeletal muscles as related to pres-

- 754 sure sore biomechanics, *Journal of Biomechanics* 39 (2006) 2725–
755 2732. URL: <https://doi.org/10.1016/j.jbiomech.2005.08.010>.
756 doi:10.1016/j.jbiomech.2005.08.010.
- 757 [13] V. Luboz, M. Bailet, C. B. Grivot, M. Rochette, B. Diot, M. Bucki,
758 Y. Payan, Personalized modeling for real-time pressure ulcer
759 prevention in sitting posture, *Journal of Tissue Viability* 27
760 (2018) 54–58. URL: <https://doi.org/10.1016/j.jtv.2017.06.002>.
761 doi:10.1016/j.jtv.2017.06.002.
- 762 [14] K. M. Moerman, M. van Vijven, L. R. Solis, E. E. van Haaften,
763 A. C. Y. Loenen, V. K. Mushahwar, C. W. J. Oomens, On the
764 importance of 3d, geometrically accurate, and subject-specific finite
765 element analysis for evaluation of in-vivo soft tissue loads, *Com-
766 puter Methods in Biomechanics and Biomedical Engineering* 20 (2016)
767 483–491. URL: <https://doi.org/10.1080/10255842.2016.1250259>.
768 doi:10.1080/10255842.2016.1250259.
- 769 [15] A. Macron, H. Pillet, J. Doridam, A. Verney, P.-Y. Rohan, Develop-
770 ment and evaluation of a new methodology for the fast generation of
771 patient-specific finite element models of the buttock for sitting-acquired
772 deep tissue injury prevention, *Journal of Biomechanics* 79 (2018)
773 173–180. URL: <https://doi.org/10.1016/j.jbiomech.2018.08.001>.
774 doi:10.1016/j.jbiomech.2018.08.001.
- 775 [16] M. Bucki, V. Luboz, A. Perrier, E. Champion, B. Diot, N. Vuillerme,
776 Y. Payan, Clinical workflow for personalized foot pressure ulcer
777 prevention, *Medical Engineering & Physics* 38 (2016) 845–
778 853. URL: <https://doi.org/10.1016/j.medengphy.2016.04.017>.
779 doi:10.1016/j.medengphy.2016.04.017.
- 780 [17] S. Niroomandi, A. Perrier, M. Bucki, Y. Payan, Real-time computer
781 modeling in prevention of foot pressure ulcer using patient-specific finite
782 element model and model order reduction techniques, in: *Innovations
783 and Emerging Technologies in Wound Care*, Elsevier, 2020, pp. 87–102.
784 URL: <https://doi.org/10.1016/b978-0-12-815028-3.00005-5>.
785 doi:10.1016/b978-0-12-815028-3.00005-5.
- 786 [18] W. van Zwam, M. van Turnhout, C. Oomens, Risk fac-
787 tors for developing heel ulcers for bedridden patients: A fi-

- 788 nite element study, *Clinical Biomechanics* 78 (2020) 105094.
 789 URL: <https://doi.org/10.1016/j.clinbiomech.2020.105094>.
 790 doi:10.1016/j.clinbiomech.2020.105094.
- 791 [19] S. Portnoy, I. Siev-Ner, N. Shabshin, A. Kristal, Z. Yizhar,
 792 A. Gefen, Patient-specific analyses of deep tissue loads post
 793 transtibial amputation in residual limbs of multiple pros-
 794 thetic users, *Journal of Biomechanics* 42 (2009) 2686–2693.
 795 URL: <https://doi.org/10.1016/j.jbiomech.2009.08.019>.
 796 doi:10.1016/j.jbiomech.2009.08.019.
- 797 [20] A. Dickinson, J. Steer, P. Worsley, Finite element analy-
 798 sis of the amputated lower limb: A systematic review and
 799 recommendations, *Medical Engineering & Physics* 43 (2017)
 800 1–18. URL: <https://doi.org/10.1016/j.medengphy.2017.02.008>.
 801 doi:10.1016/j.medengphy.2017.02.008.
- 802 [21] E. Ramasamy, O. Avci, B. Dorow, S.-Y. Chong, L. Gizzi, G. Stei-
 803 dle, F. Schick, O. Röhrle, An efficient modelling-simulation-
 804 analysis workflow to investigate stump-socket interaction using patient-
 805 specific, three-dimensional, continuum-mechanical, finite element resid-
 806 ual limb models, *Frontiers in Bioengineering and Biotechnol-*
 807 *ogy* 6 (2018). URL: <https://doi.org/10.3389/fbioe.2018.00126>.
 808 doi:10.3389/fbioe.2018.00126.
- 809 [22] R. M. A. Al-Dirini, M. P. Reed, J. Hu, D. Thewlis, Development and
 810 validation of a high anatomical fidelity FE model for the buttock and
 811 thigh of a seated individual, *Annals of Biomedical Engineering* 44 (2016)
 812 2805–2816. URL: <https://doi.org/10.1007/s10439-016-1560-3>.
 813 doi:10.1007/s10439-016-1560-3.
- 814 [23] M. Van Looke, C. Simms, C. Lyons, Viscoelastic prop-
 815 erties of passive skeletal muscle in compression—cyclic be-
 816 haviour, *Journal of Biomechanics* 42 (2009) 1038–1048.
 817 URL: <https://doi.org/10.1016/j.jbiomech.2009.02.022>.
 818 doi:10.1016/j.jbiomech.2009.02.022.
- 819 [24] C. K. Simms, M. V. Looke, C. G. Lyons, SKELETAL
 820 MUSCLE IN COMPRESSION: MODELING APPROACHES
 821 FOR THE PASSIVE MUSCLE BULK, *International Journal*

- 822 for Multiscale Computational Engineering 10 (2012) 143–154.
 823 URL: <https://doi.org/10.1615/intjmultcompeng.2011002419>.
 824 doi:10.1615/intjmultcompeng.2011002419.
- 825 [25] B. B. Wheatley, R. B. Pietsch, T. L. H. Donahue, L. N.
 826 Williams, Fully non-linear hyper-viscoelastic modeling of skeletal
 827 muscle in compression, Computer Methods in Biomechanics and Biomedical Engineering 19 (2015) 1181–1189.
 828 URL: <https://doi.org/10.1080/10255842.2015.1118468>.
 829 doi:10.1080/10255842.2015.1118468.
- 831 [26] G. Sjogaard, B. Saltin, Extra- and intracellular water
 832 spaces in muscles of man at rest and with dynamic exercise,
 833 American Journal of Physiology-Regulatory, Integrative and Comparative Physiology 243 (1982) R271–R280.
 834 URL: <https://doi.org/10.1152/ajpregu.1982.243.3.R271>.
 835 doi:10.1152/ajpregu.1982.243.3.R271, pMID: 7114288.
- 837 [27] O. A. Gimnich, J. Singh, J. Bismuth, D. J. Shah, G. Brunner, Magnetic
 838 resonance imaging based modeling of microvascular perfusion in pa-
 839 tients with peripheral artery disease, Journal of Biomechanics 93 (2019)
 840 147–158. URL: <https://doi.org/10.1016/j.jbiomech.2019.06.025>.
 841 doi:10.1016/j.jbiomech.2019.06.025.
- 842 [28] M. Argoubi, A. Shirazi-Adl, Poroelastic creep response analysis of a lum-
 843 bar motion segment in compression, Journal of Biomechanics 29 (1996)
 844 1331–1339. URL: [https://doi.org/10.1016/0021-9290\(96\)00035-8](https://doi.org/10.1016/0021-9290(96)00035-8).
 845 doi:10.1016/0021-9290(96)00035-8.
- 846 [29] M. Peyrounette, Y. Davit, M. Quintard, S. Lorthois, Multiscale mod-
 847 elling of blood flow in cerebral microcirculation: Details at capillary
 848 scale control accuracy at the level of the cortex, PLOS ONE 13 (2018)
 849 e0189474. URL: <https://doi.org/10.1371/journal.pone.0189474>.
 850 doi:10.1371/journal.pone.0189474.
- 851 [30] J. Siddique, A. Ahmed, A. Aziz, C. Khalique, A review of mix-
 852 ture theory for deformable porous media and applications, Applied
 853 Sciences 7 (2017) 917. URL: <https://doi.org/10.3390/app7090917>.
 854 doi:10.3390/app7090917.

- [31] M. Hosseini-Farid, M. Ramzanpour, J. McLean, M. Ziejewski, G. Karami, A poro-hyper-viscoelastic rate-dependent constitutive modeling for the analysis of brain tissues, *Journal of the Mechanical Behavior of Biomedical Materials* 102 (2020) 103475. URL: <https://doi.org/10.1016/j.jmbbm.2019.103475>. doi:10.1016/j.jmbbm.2019.103475.
- [32] G. Franceschini, D. Bigoni, P. Regitnig, G. Holzapfel, Brain tissue deforms similarly to filled elastomers and follows consolidation theory, *Journal of the Mechanics and Physics of Solids* 54 (2006) 2592–2620. URL: <https://doi.org/10.1016/j.jmps.2006.05.004>. doi:10.1016/j.jmps.2006.05.004.
- [33] G. Sciumè, D. P. Boso, W. G. Gray, C. Cobelli, B. A. Schrefler, A two-phase model of plantar tissue: a step toward prediction of diabetic foot ulceration, *International Journal for Numerical Methods in Biomedical Engineering* 30 (2014) 1153–1169. URL: <https://onlinelibrary.wiley.com/doi/abs/10.1002/cnm.2650>. doi:<https://doi.org/10.1002/cnm.2650>. arXiv:<https://onlinelibrary.wiley.com/doi/pdf>
- [34] S. Urcun, P.-Y. Rohan, W. Skalli, P. Nassoy, S. P. A. Bordas, G. Sciumè, Digital twinning of cellular capsule technology: Emerging outcomes from the perspective of porous media mechanics, *PLOS ONE* 16 (2021) 1–30. URL: <https://doi.org/10.1371/journal.pone.0254512>. doi:10.1371/journal.pone.0254512.
- [35] G. Sciumè, S. Shelton, W. G. Gray, C. T. Miller, F. Hussain, M. Ferrari, P. Decuzzi, B. A. Schrefler, A multiphase model for three-dimensional tumor growth, *New Journal of Physics* 15 (2013) 015005. URL: <https://doi.org/10.1088/1367-2630/15/1/015005>. doi:10.1088/1367-2630/15/1/015005.
- [36] G. Sciumè, Mechanistic modeling of vascular tumor growth: an extension of biot’s theory to hierarchical bi-compartment porous medium systems, *Acta Mechanica* 232 (2021) 1445–1478. URL: <https://doi.org/10.1007/s00707-020-02908-z>. doi:10.1007/s00707-020-02908-z.
- [37] W. G. Gray, C. T. Miller, Introduction to the Thermodynamically Constrained Averaging Theory for Porous Medium

- 889 Systems, Springer International Publishing, 2014. URL:
890 <https://doi.org/10.1007/978-3-319-04010-3>. doi:10.1007/978-
891 3-319-04010-3.
- 892 [38] P. Mascheroni, C. Stigliano, M. Carfagna, D. P. Boso, L. Preziosi,
893 P. Decuzzi, B. A. Schrefler, Predicting the growth of glioblastoma
894 multiforme spheroids using a multiphase porous media model, *Biome-*
895 *chanics and Modeling in Mechanobiology* 15 (2016) 1215–1228. URL:
896 <https://doi.org/10.1007/s10237-015-0755-0>. doi:10.1007/s10237-
897 015-0755-0.
- 898 [39] A. J. Vaidya, B. B. Wheatley, An experimental and computa-
899 tional investigation of the effects of volumetric boundary conditions
900 on the compressive mechanics of passive skeletal muscle, *Journal*
901 *of the Mechanical Behavior of Biomedical Materials* 102 (2020)
902 103526. URL: <https://doi.org/10.1016/j.jmbbm.2019.103526>.
903 doi:10.1016/j.jmbbm.2019.103526.
- 904 [40] M. Viceconti, S. Olsen, L.-P. Nolte, K. Burton, Extracting clin-
905 ically relevant data from finite element simulations 20 (2005) 451–
906 454. URL: <https://doi.org/10.1016/j.clinbiomech.2005.01.010>.
907 doi:10.1016/j.clinbiomech.2005.01.010.
- 908 [41] I. Abaqus, Abaqus documentation, Version 6 (2014) 1–5.
- 909 [42] D. A. Sleboda, T. J. Roberts, Incompressible fluid plays a mechanical
910 role in the development of passive muscle tension, *Biology Letters* 13
911 (2017) 20160630. URL: <https://doi.org/10.1098/rsbl.2016.0630>.
912 doi:10.1098/rsbl.2016.0630.
- 913 [43] B. B. Wheatley, G. M. Odegard, K. R. Kaufman, T. L. H. Donahue, A
914 validated model of passive skeletal muscle to predict force and intramus-
915 cular pressure, *Biomechanics and Modeling in Mechanobiology* 16 (2016)
916 1011–1022. URL: <https://doi.org/10.1007/s10237-016-0869-z>.
917 doi:10.1007/s10237-016-0869-z.
- 918 [44] C. Oomens, W. Zenhorst, M. Broek, B. Hemmes, M. Poeze,
919 P. Brink, D. Bader, A numerical study to analyse the risk
920 for pressure ulcer development on a spine board 28 (2013) 736–
921 742. URL: <https://doi.org/10.1016/j.clinbiomech.2013.07.005>.
922 doi:10.1016/j.clinbiomech.2013.07.005.

- 923 [45] W. A. Traa, M. C. van Turnhout, K. M. Moerman, J. L. Nelissen,
924 A. J. Nederveen, G. J. Strijkers, D. L. Bader, C. W. J. Oomens, MRI
925 based 3d finite element modelling to investigate deep tissue injury, *Com-
926 puter Methods in Biomechanics and Biomedical Engineering* 21 (2018)
927 760–769. URL: <https://doi.org/10.1080/10255842.2018.1517868>.
928 doi:10.1080/10255842.2018.1517868.
- 929 [46] W. Lee, B. H. Won, S. W. Cho, Finite element model-
930 ing for predicting the contact pressure between a foam mat-
931 tress and the human body in a supine position 20 (2016)
932 104–117. URL: <https://doi.org/10.1080/10255842.2016.1203421>.
933 doi:10.1080/10255842.2016.1203421.
- 934 [47] M. Verver, J. van Hoof, C. Oomens, J. Wismans, F. Baai-
935 jens, A finite element model of the human buttocks for
936 prediction of seat pressure distributions 7 (2004) 193–203.
937 URL: <https://doi.org/10.1080/10255840410001727832>.
938 doi:10.1080/10255840410001727832.
- 939 [48] A. Levy, K. Kopplin, A. Gefen, Simulations of skin and
940 subcutaneous tissue loading in the buttocks while regaining
941 weight-bearing after a push-up in wheelchair users 28 (2013)
942 436–447. URL: <https://doi.org/10.1016/j.jmbbm.2013.04.015>.
943 doi:10.1016/j.jmbbm.2013.04.015.
- 944 [49] R. Sopher, J. Nixon, C. Gorecki, A. Gefen, Exposure to inter-
945 nal muscle tissue loads under the ischial tuberosities during sitting
946 is elevated at abnormally high or low body mass indices 43 (2010)
947 280–286. URL: <https://doi.org/10.1016/j.jbiomech.2009.08.021>.
948 doi:10.1016/j.jbiomech.2009.08.021.
- 949 [50] T. Zeevi, A. Levy, N. Brauner, A. Gefen, Effects of ambient
950 conditions on the risk of pressure injuries in bedridden patients-
951 multi-physics modelling of microclimate 15 (2017) 402–416. URL:
952 <https://doi.org/10.1111/iwj.12877>. doi:10.1111/iwj.12877.
- 953 [51] L.-L. Gras, D. Mitton, N. Crevier-Denoix, S. Laporte, The non-
954 linear response of a muscle in transverse compression: assessment
955 of geometry influence using a finite element model, *Computer
956 Methods in Biomechanics and Biomedical Engineering* 15 (2012)

- 13–21. URL: <https://doi.org/10.1080/10255842.2011.564162>.
doi:10.1080/10255842.2011.564162.
- [52] V. Klika, E. A. Gaffney, Y.-C. Chen, C. P. Brown, An overview of multiphase cartilage mechanical modelling and its role in understanding function and pathology, *Journal of the Mechanical Behavior of Biomedical Materials* 62 (2016) 139–157. URL: <https://www.sciencedirect.com/science/article/pii/S1751616116301047>.
doi:<https://doi.org/10.1016/j.jmbbm.2016.04.032>.
- [53] S. C. Cowin, Bone poroelasticity, *Journal of Biomechanics* 32 (1999) 217–238. URL: <https://www.sciencedirect.com/science/article/pii/S0021929098001614>.
doi:[https://doi.org/10.1016/S0021-9290\(98\)00161-4](https://doi.org/10.1016/S0021-9290(98)00161-4).
- [54] C. Hellmich, F.-J. Ulm, Drained and undrained poroelastic properties of healthy and pathological bone: A poro-micromechanical investigation 58 (2005) 243–268. URL: <https://doi.org/10.1007/s11242-004-6298-y>. doi:10.1007/s11242-004-6298-y.
- [55] B. B. Wheatley, G. M. Odegard, K. R. Kaufman, T. L. H. Donahue, A case for poroelasticity in skeletal muscle finite element analysis: experiment and modeling, *Computer Methods in Biomechanics and Biomedical Engineering* 20 (2016) 598–601. URL: <https://doi.org/10.1080/10255842.2016.1268132>.
doi:10.1080/10255842.2016.1268132.
- [56] G. Sjogaard, B. Saltin, Extra- and intracellular water spaces in muscles of man at rest and with dynamic exercise 243 (1982) R271–R280. URL: <https://doi.org/10.1152/ajpregu.1982.243.3.r271>.
doi:10.1152/ajpregu.1982.243.3.r271.
- [57] M. A. Soltz, G. A. Ateshian, Experimental verification and theoretical prediction of cartilage interstitial fluid pressurization at an impermeable contact interface in confined compression, *Journal of Biomechanics* 31 (1998) 927–934. URL: [https://doi.org/10.1016/s0021-9290\(98\)00105-5](https://doi.org/10.1016/s0021-9290(98)00105-5).
doi:10.1016/s0021-9290(98)00105-5.

990 [58] Tavenas, F., Brucy, M., Magnan, J.-P., La Rochelle, P., Roy,
991 M., Analyse critique de la théorie de consolidation uni-
992 dimensionnelle de terzaghi, Rev. Fr. Geotech. (1979) 29–
993 43. URL: <https://doi.org/10.1051/geotech/1979007029>.
994 doi:10.1051/geotech/1979007029.